Water depth–terrigenous input dynamic equilibrium controls the Eocene lacustrine shale laminae records in Jiyang depression, Bohai Bay Basin, East China

Chao Liang, Yingchang Cao, Jing Wu, Yu Han, Keyu Liu, Fang Hao, Danish Khan, Junfang Mei, Shun Zhang, and Yong Wang

ABSTRACT

Lacustrine organic-rich Eocene shales are well developed within the faulted lake basin in the Bohai Bay Basin in eastern China. It is crucial to comprehend the sedimentation of these shales for the study of depositional processes, paleoenvironment reconstruction, and shale oil exploration. This research investigates the sedimentary characteristics and formation mechanisms of lacustrine shales in the upper fourth member and lower third member of the Eocene Shahejie Formation (Es4s–Es3x shale), based on thin sections and field-emission scanning electron microscopy observations of well cores, with x-ray diffraction analysis, electron probe microanalysis, and geochemical elements analysis. The Es4s–Es3x shale is deposited in a hypoxic saline lake with laminated, massive, and lenticular sedimentary structures, wherein laminated shale is the dominant lithofacies. Eight laminae units have been identified: micritic calcite laminae (MCAL), sparry calcite laminae (SCAL), quartz–feldspar–clay mixed laminae (QFCL), organic-rich clay laminae (OCL), clay laminae (CL), organic matter laminae (OL), dolomite laminae (DL), and anhydrite laminae (AL). They form seven lamina couplets: MCAL + OL + CL, QFCL + OCL, SCAL + OCL, SCAL + OL, MCAL + QFCL, DL + OCL, and DL + AL. Moreover, three massive lithofacies have been identified: massive siltstone and claystone, massive limestone/silty limestone, and massive dolomite. Three calcite lenticular laminae have also been

---

Manuscript received September 15, 2021; provisional acceptance January 3, 2022; revised manuscript received August 31, 2022; revised manuscript provisional acceptance November 30, 2022; 2nd revised manuscript received January 17, 2023; final acceptance February 25, 2023.
DOI:10.1306/07052321160

AUTHORS

CHAO LIANG ~ *Key Laboratory of Deep Oil and Gas, School of Geosciences, China University of Petroleum (East China), Qingdao, China; Laboratory for Marine Mineral Resource, Qingdao National Laboratory for Marine Science and Technology, Qingdao, China; liangchao0318@163.com; liangchao0318@upc.edu.cn*

Chao Liang is is a professor at China University of Petroleum. He received his Ph.D. from China University of Geosciences (Beijing) in 2015. His research focuses on shale sedimentology, sequence stratigraphy, shale diagenesis, and shale reservoir quality prediction.

YINGCHANG CAO ~ *Key Laboratory of Deep Oil and Gas, School of Geosciences, China University of Petroleum (East China), Qingdao, China; Laboratory for Marine Mineral Resource, Qingdao National Laboratory for Marine Science and Technology, Qingdao, China; caoych@upc.edu.cn*

Yingchang Cao is a professor at China University of Petroleum. His research interests lie in the fields of sequence stratigraphy, sedimentology, and sandstone reservoir quality prediction.

JING WU ~ *Laboratory for Marine Mineral Resource, Qingdao National Laboratory for Marine Science and Technology, Qingdao, China; Shandong Key Laboratory of Depositional Mineralization and Sedimentary Mineral, Shandong University of Science and Technology, Qingdao, China; wujing6524982@163.com*

Jing Wu is a professor at Shandong University of Science and Technology. She received her Ph.D. from China University of Geosciences (Beijing) in 2015. Her research focuses on shale sedimentology and sequence stratigraphy.

YU HAN ~ *Key Laboratory of Deep Oil and Gas, School of Geosciences, China University of Petroleum (East China), Qingdao, China; B20010017@s.upc.edu.cn*

Yu Han is currently a Ph.D. student at China University of Petroleum. His research focuses on shale sedimentology and cyclostratigraphy.

KEYU LIU ~ *Key Laboratory of Deep Oil and Gas, School of Geosciences, China University of Petroleum (East China), Qingdao, China; Laboratory for Marine Mineral Resource, Qingdao National Laboratory for Marine Science and Technology, Qingdao, China; liukeyu@upc.edu.cn*

Keyu Liu is a professor at China University of Petroleum and an adjunct research fellow at Commonwealth Scientific and Industrial Research Organisation and Curtin University, Australia, working on sedimentology and petroleum system analysis.

FANG HAO ~ *Key Laboratory of Deep Oil and Gas, School of Geosciences, China University of Petroleum (East China), Qingdao, China; Laboratory for Marine Mineral Resource, Qingdao National Laboratory for Marine Science and Technology, Qingdao, China; haofang@upc.edu.cn*

Fang Hao is a professor at China University of Petroleum. His research focuses on hydrocarbon accumulation mechanisms and unconventional petroleum geology.

DANISH KHAN ~ *Key Laboratory of Deep Oil and Gas, School of Geosciences, China University of Petroleum (East China), Qingdao, China; danish20124@yahoo.com*

Danish Khan is a Ph.D. student at China University of Petroleum. His research focuses on sedimentology and petroleum geology.

JUNFANG MEI ~ *Key Laboratory of Deep Oil and Gas, School of Geosciences, China University of Petroleum (East China), Qingdao, China; s21010031@s.upc.edu.cn*

Junfang Mei is a master's student at China University of Petroleum. Her research interests lie in fine-grained sedimentology.

SHUN ZHANG ~ *Geological Scientific Research Institute, Sinopec Shengli Oilfield, Dongying, China; satisfactoryshun@163.com*

identified. The Sr/Ba, S/total organic carbon, and Th/U ratios and other geochemical elements show that Es4s–Es3x shale is deposited in the hypoxic saline lake. Factors such as lake water, salinity, oxidation reduction, and water depth all vary with episodic high frequency. The lithology, lithofacies sequence, and geochemical characteristics denote that the laminated shale was deposited via suspension. The halocline in the lake is a key factor controlling the lacustrine laminae deposition and the lamina couplet distribution in the lake basin. The halocline location fluctuations are controlled by the dynamic equilibrium of the water depth and terrigenous input, which further control the development of different laminae and lamina couplets. Massive mudstone formed due to turbidity, debris flows, and evaporation. The MCAL may have been deposited due to breakdown and resuspension under strong hydrodynamics. Additionally, erosion, deposition, and compaction of water-rich muds and biodisturbance control the formation of the three lenses.

INTRODUCTION

Shale makes up approximately two-thirds of the sedimentary deposits and is a natural archive of paleoenvironmental conditions (Stow and Mayall, 2000; Schieber et al., 2007; Aplin and Macquaker, 2011). Shale comprises a variable mixture of clay minerals, quartz, feldspars, carbonates, sulfides, amorphous material, and organic matter (OM), and it is an important petroleum source, a reservoir for shale oil and gas, and seals in conventional reservoirs (Macquaker and Adams, 2003; Loucks and Ruppel, 2007; Macquaker et al., 2010; Milliken, 2014; Lazar et al., 2015; Ilgen et al., 2017; Li et al., 2021). The depositional processes leading to shales mostly involve pelagic settings, hemipelagic sedimentation, turbidity currents, debris flows, slides, and wave-enhanced sediment gravity flows; one or more of these processes may contribute to the deposition of black shale (Stow and Bowen, 1980; Arthur and Sageman, 1994; Stow et al., 2001; Petter and Steel, 2006; Soyinka and Slatt, 2008; Piper and Calvert, 2009; Macquaker et al., 2010; Ghadeer and Macquaker, 2011). The different depositional processes result in differences in lithofacies, lithofacies combination, mineral and element abundance, OM enrichment, OM minerals occurrence, and reservoir heterogeneity of shale oil and gas (Watanabe and Akiyama, 1998; Ochoa et al., 2013; Konitzer et al., 2014; Plint, 2014; Frébourg et al., 2016; Rimstidt et al., 2017).

Laminated shale is one of the most common lithofacies. Flume experiments have demonstrated that laminated black shales can accumulate under energetic and oxygenated conditions (Schieber and Southard, 2009; Schieber, 2011, 2016; Schieber et al., 2013). Despite the existence of false laminar sediments formed by the flocculation transport and deposition process (Schieber et al., 2007, 2010; Schieber and Southard, 2009), laminated shale is considered to provide considerably detailed information for reconstructing the paleoclimate and paleoocean/-lake environment (Cheel, 1990; Hatch and Leventhal, 1992; Algeo and Maynard, 2004; Macquaker et al., 2007). Varves stem from sediment supply differences caused by seasonal climate (e.g., in Baltic Sea varves); diatom mud laminae are deposited during the spring and summer, and clay-rich mud laminae are deposited during the autumn and winter (Burke et al., 2002; Kotilainen et al., 2007; Jokinen et al., 2015; Roop et al., 2015). The formation of a modern ocean or lake varve is indicative of several conditions, including the bottom of the dissolved oxygen depletion layer, large deposition rate, and seasonal differences in the sediment input, intensity, and depth of the oxygen minimum zone (Ojala et al., 2012; Zolitschka et al., 2015; Schimmelmann et al., 2016). Additionally, geomorphology, chemical properties of the bedrock, amount of insolation, precipitation, and evaporation all affect the formation of lacustrine varves (Zolitschka and Enters, 2009; Ebert and Trauth, 2015). Varve formation is controlled by differences in seasonal sediment supply; therefore, obtaining detailed laminae information from mud sedimentary records is essential for studying the paleoclimate reconstruction.

In mud sedimentary records, laminae components, lamina couplet (LC) types, and the pattern in which they combine in the vertical direction commonly and rapidly change, especially in the lake basin. This is due to the high-frequency evolution of climatic and paleolimnological conditions, which reflects more complex and sensitive basin depositional systems than those in the marine environment (Burton et al., 2014; Deocampo et al., 2017; Xia et al., 2019a; Cao et al., 2020). Additionally, the laminae type, origin, and driving mechanism need to be understood to analyze the paleolimnology and its response sensitivity to the climate as well as to compare the depositional response differences of marine and lake basins to the climate (Thiry, 2000; Tindall et al., 2010; Tänavsuu-Milkeviciene and Sarg, 2012; Deocampo et al., 2017; Xia et al., 2019b). Lacustrine shales are the main exploration targets for shale oil in China, and analyzing the formation and distribution of shales is crucial for predicting favorable target areas for shale oil (Zou et al., 2019).

The study intervals in this research are 500-m-thick successive sequences in the upper fourth member and lower third member of the Shahejie Formation (Es4s–Es3x) of the Eocene, which reportedly were deposited during the Middle Eocene climate optimum. Literature suggests that the warm and humid paleoclimate of this period promoted bioactivity, provided abundant paleoproductivity, and formed the most important source rocks in Bohai Bay Basin, East Asia (Shi et al., 2018). This study aims to (1) determine the laminae types, LC types, and lithofacies of

Shun Zhang is a senior engineer at Sinopec Shengli Oilfield. His research focuses on sedimentology and reservoir geology.

YONG WANG ~ *Geological Scientific Research Institute, Sinopec Shengli Oilfield, Dongying, China; wangyong731.slyt@sinopec.com*

Yong Wang is a senior engineer at Sinopec Shengli Oilfield. His research interests lie in reservoir geology and oil-gas exploration.

ACKNOWLEDGMENTS

The research presented in this paper was supported by the Shandong Provincial Key Research and Development Program, China (2020ZLYS08), the National Natural Science Foundation of China (Nos. 42272119, 42072164, 41821002), Taishan Scholars Program, China (No. TSQN201812030), and the Fundamental Research Funds for the Central Universities, China (2022CX06001A).

lacustrine shale; (2) analyze the formation mechanism of lacustrine shale of Eocene shale records; and (3) discuss the paleoclimatic and paleolimnological significance of the shale laminae.

GEOLOGICAL SETTING

Bohai Bay Basin is a typical fault-depression lake basin that developed in the Paleozoic North China craton basement because of the subduction of the Indian and Pacific plates under the Eurasian plate, which is filled with Mesozoic–Cenozoic continental strata (Lin et al., 2009; Liang et al., 2018). The Jiyang depression is a Mesozoic–Cenozoic rift depression in the southeastern part of the Bohai Bay Basin (Figure 1A), which is bordered by the Tanlu fault belt in the east, the Chengning uplift area in the northwest, and the Luxi uplift in the south (Figure 1B). The Jiyang depression includes four secondary depressions: the Dongying, Huimin, Zhanhua, and Chezhen depressions, which are divided by the Qingcheng, Chenjiazhuang, and Yihezhuang uplifts (Figure 1B). The basin underwent two tectonic episodic periods: rifting (65–24.6 Ma) and thermal subsidence (24.6 Ma–present) (Liu et al., 2004; Li et al., 2007; Yang et al., 2009). The rifting stage can be further divided into four episodic periods (Figure 2): the initial period (rifting I), development period (rifting II), peak period (rifting III), and atrophy period (rifting IV). The corresponding sedimentary environment changed from shallow lake to semideep lake and further to fluvial delta, with as much as 8000 m of lacustrine sediments deposited (Figure 2), comprising Cenozoic basin-filling strata, including the Kongdian (Ek), Shahejie (Es), Dongying (Ed), Guantao (Ng), Minghuazhen (Nm), and Pingyuan (Qp) Formations. The Shahejie Formation can be subdivided into four members from the top to bottom: Es1, Es2, Es3, and Es4 (Figure 2). The Es3 can be further subdivided into three submembers (from the top to bottom): Es3s, Es3z, and Es3x. The Es4 can be further subdivided into two submembers: Es4s and Es4x (Figure 2). At circa 42 Ma (corresponding to the early Lutetian Stage), the lake basin quickly subsided with a large-scale lake expansion, reaching a maximum in the Es4s and Es3x periods (Qiu et al., 2006; Shi et al., 2019), and a semiclosed saline lake environment with anoxic conditions formed at the lake bottom (Chen et al., 2018; Liang et al., 2018). Subsequently, approximately 500-m-thick organic-rich Es4s–Es3x black shale was deposited, which is the largest deposit of source rocks in the Jiyang depression and in the entire Bohai Bay Basin (Figure 3). Studies suggest that the warm and humid paleoclimate promoted bioactivity, provided abundant paleoproductivity, and resulted in high total organic carbon (*TOC*) content (average of 3.17%). Relative to the background of the salinized lake basin (Wei et al., 2018), the shale comprises well-developed laminae with a high content of carbonate minerals.

SAMPLES AND METHODS

The basic data presented here include data of 1000-m core from four wells (i.e., L69, FY1, NY1, and LY1; see Figure 1B, C) as well as 1136 thin sections, 78 field-emission scanning electron microscopy (FE-SEM) samples, x-ray diffraction (XRD) data from wells NY1 and L69 that were collected at approximately 0.25-m intervals, and geochemical element analysis data from well NY1 that were collected at approximately 1.0-m intervals. All thin-section observations were made using a Zeiss microscope Axio Scope A1 for 0.03-mm-thick samples. Mineral XRD was performed using a D/max-2500 TTR. Prior to analysis, each sample was oven dried at 40°C for 2 days and ground to <40 mm using an agate mortar to thoroughly disperse the minerals. Subsequent computer diffractogram analysis enabled the identification and semiquantitative investigation of the relative abundances (weight percent) of the various mineral phases, whereas *TOC* was determined using a LECO carbon-sulfur analyzer CS600 at a test temperature of 27°C. The measurement technique used here is based on sample combustion in an O_2 atmosphere for converting *TOC* to CO_2 (Charles and Simmons, 1986).

Electron microprobe analyses were conducted using a JEOL JXA-8230 system, with carbon-coated samples. These analyses were performed under room temperature conditions at 25°C and 40% humidity. The beam was operated at 15 kV and a beam current of 20 nA, and the beam diameter was 5–8 μm for the laminae in shales.

The geochemical characteristics of the samples were determined using an x-ray fluorescence spectrometer with an analytical uncertainty of less than 3%.

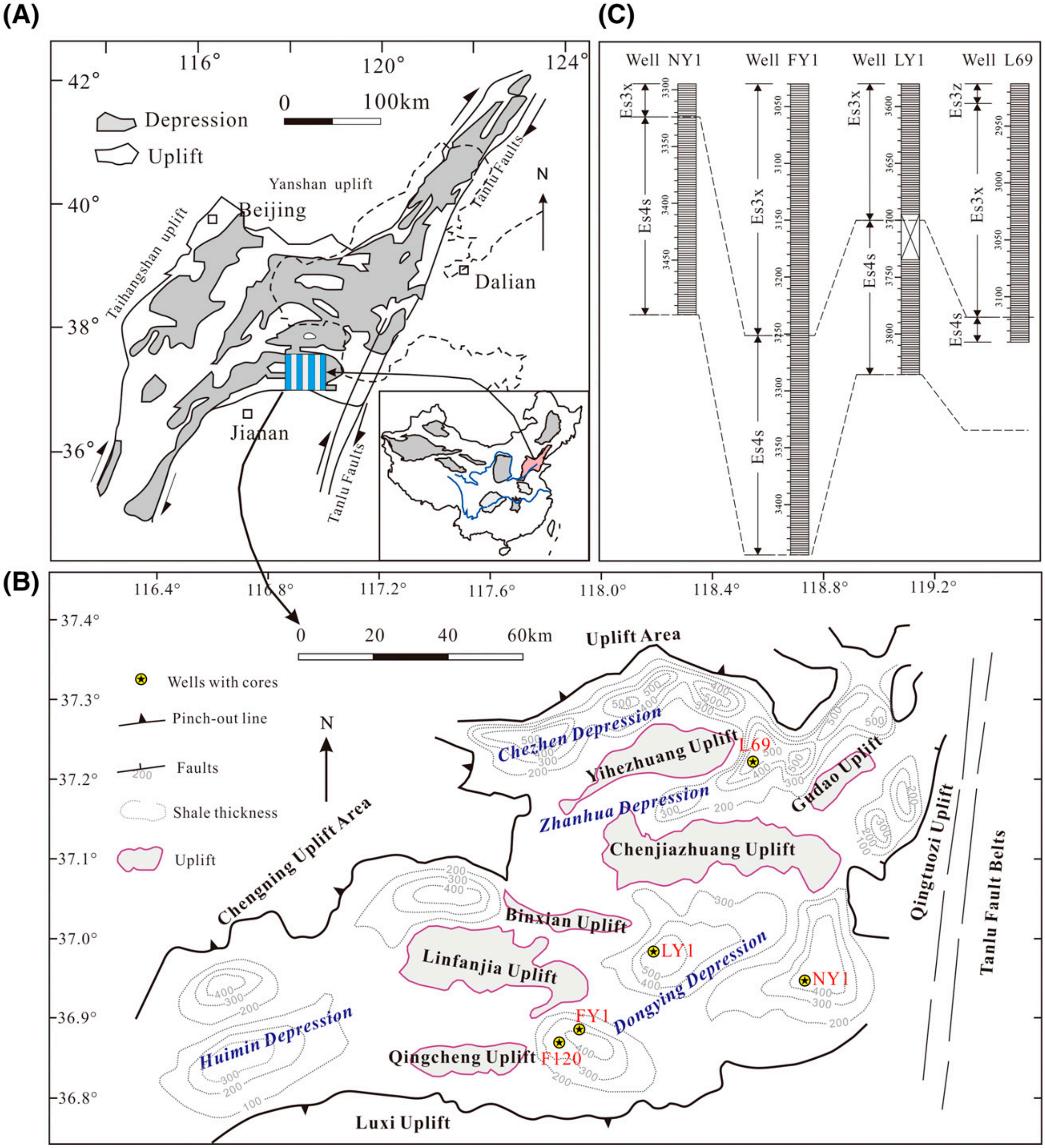

Figure 1. Regional index map showing the study area. (A) Structural map of Bohai Bay Basin and the location of the Jiyang depression (box). (B) Structural map showing key well locations in the Jiyang depression. (C) Core stratigraphy and depth in meters of key wells. Well locations are shown in (B). Es4s = upper fourth member of Shahejie Formation; Es3x = lower third member of Shahejie Formation; Es3z = middle third member of Shahejie Formation.

Samples were ground using 200 mesh and subjected to inductively coupled plasma-atomic emission spectroscopy (JY38S) with emphasis on the following elements: Al, Ba, Cr, Fe, Mg, Na, Sr, Th, and U. Ambient temperature was held between 70°C and 75°C for all analyses, and relative humidity was less than 70%. All measurements were obtained as weight percent and are reported throughout as percent.

The Ar ion-beam milling was used to prepare samples for nanopore imaging, and high-resolution

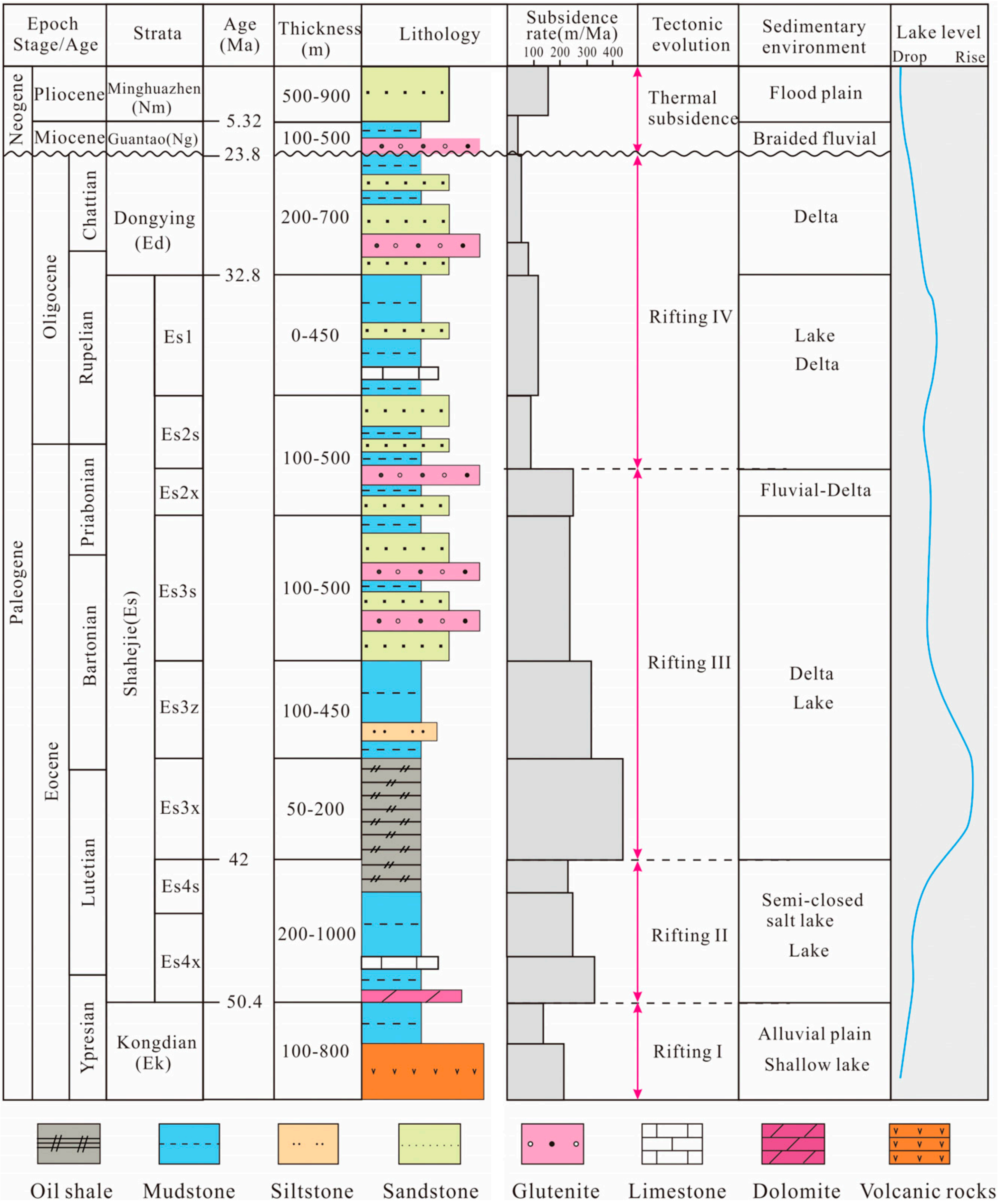

Figure 2. Sedimentary facies and stratigraphic column of the Jiyang depression (modified from Ren and Zhang, 2004; Liang et al., 2018; Shi et al., 2019).

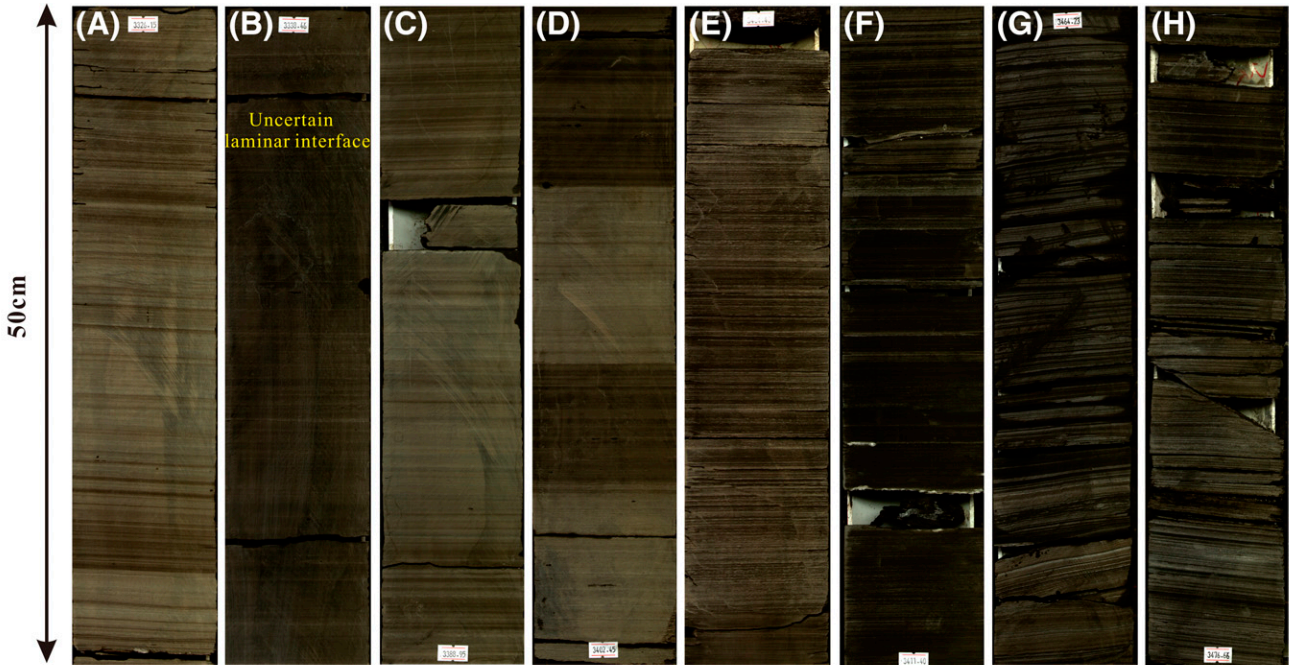

Figure 3. Core characteristics of laminated shale in well NY1. (A) Light gray calcareous shale, 3326.15–3326.65 m. (B) Black organic-rich shale with indistinct laminar interface, 3338.46–3338.96 m. (C) Light gray calcareous shale with unclear laminar interface, 3383.45–3383.95 m. (D) Light gray calcareous shale interbedded with black calcareous shale, single lithofacies thickness approximately 10–15 cm, 3401.95–3402.45 m. (E) Black argillaceous shale with clear laminar interface, 3404.46–3404.96 m. (F) Black argillaceous shale with clear laminar interface, 3410.90–3411.40 m. (G) Black calcareous shale with clear laminar interface, 3464.23–3464.73 m. (H) Black dolomite shale with clear laminar interface, 3476.16–3476.66 m.

FE-SEM was employed to observe micro- and nano-sized pores. All samples were gold coated and imaged using a Hitachi S-4800 (FE-SEM equipment) with a working current of 10 kV. The lithology and mineralogy of the target-layer intervals in the study area were based on detailed observations of the cores, thin sections, SEM observations, and whole-rock and clay mineral XRD analyses.

Geochemical elements were used to analyze the sedimentary environments, wherein Sr/Ba and S/*T*OC ratios were used as proxies for paleosalinity (Wei and Algeo, 2020), pyrite and organic carbon/phosphorus (C_{org}/P) ratios (Algeo and Ingall, 2007) were used as proxies for anoxic conditions, and Co, Cr, K, Ni, Al, Ti, and Na values and the Fe/Mn ratio were used as proxies for sediment provenance. The laminae were comprehensively identified in the 3440–3500 m interval, where four thin sections were collected every meter. The lamina type and thickness were counted from an average of 20 to 30 photomicrographs for each thin section. To better understand the formation of these laminae and laminae combinations, we performed electron probe microanalysis line scans of the elements comprising the seven LCs.

RESULTS

Mineral Composition

The XRD results suggest that the Es4s–Es3x shale predominately comprises carbonate and clay minerals as well as quartz and nominally comprises plagioclase, K-feldspar, and pyrite, wherein calcite is the dominant mineral (average of 39.1%). Compared to Es3x shale, the Es4s shale has a relatively high calcite content (Figure 4). Its average clay mineral content is approximately 21.2%, dominated by illite (average of 83.8%), although some illite–smectite mixed layer is present (average of 15.2%). Quartz is also common, ranging between 1% and 54%, with an average of 22.9%. Plagioclase content ranges from 1% to 22% (average of 5.8%), whereas pyrite content ranges from 1% to 13% (average of 3.9%).

Lithofacies

Laminated Shales

In the laminated shale, eight lamina types are identified: micritic calcite laminae (MCAL), sparry calcite laminae (SCAL), quartz–feldspar–clay mixed

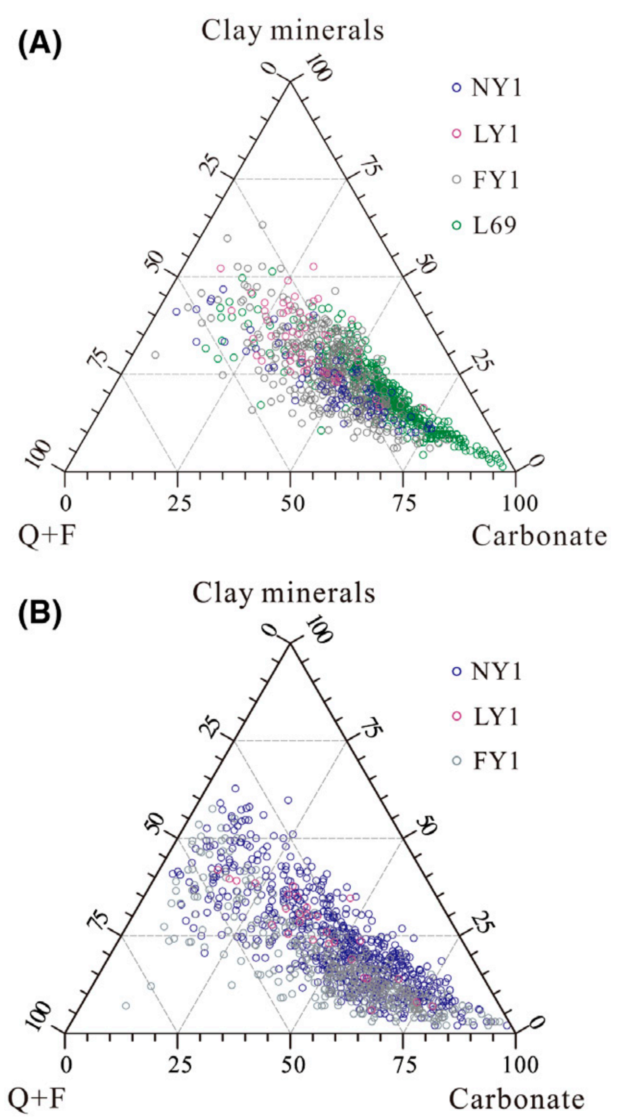

Figure 4. Ternary plot of the whole-rock mineral composition (percent) of the lower third member of Shahejie Formation (A) and the upper fourth member of Shahejie Formation (B) shales in the study area. Well (NY1, LY1, FY1, and L69) locations are shown in Figure 1C. F = feldspar; Q = quartz.

laminae (QFCL), organic-rich clay laminae (OCL), OM laminae (OL), clay laminae (CL), dolomite laminae (DL), and anhydrite laminae (AL). Furthermore, seven types of LCs can be identified (Table 1):

1. MCAL + OL + CL comprises three units: (a) MCAL algal filament with a thickness of 60–150 μm and abrupt contact with the underlying CL, which is characterized by internal gradients with filaments; (b) OL with a thickness of 5–10 μm and a clear laminar boundary; and (c) CL with a thickness of 40–100 μm, which is deposited on the underlying OL and up to the A unit of another MCAL + OL + CL (Figure 5A).
2. QFCL + OCL: OM is mixed with clay minerals in the OCL and quartz particles, as can be seen in the QFCL (Figure 5B).
3. SCAL + OCL: the laminae units comprise pure components with clear laminar boundaries. The units have rare terrigenous inputs and no biological shell fragments, with thick SCAL (50–200 μm) and thin OCL (10–40 μm) (Figure 5C).
4. SCAL + OL: similar to SCAL + OCL, the laminae units comprise pure components with clear laminar boundaries. The units have rare terrigenous inputs and no biological shell fragments, with thick SCAL (50–150 μm) and thin OL (5–20 μm) (Figure 5D).
5. MCAL + QFCL: QFCL units are rich in ostracod fragments and MCAL is lenticular, suggesting a relatively strong hydrodynamic force and terrigenous inputs, with carbonate laminae modification (Figure 5E).
6. DL + OCL: the thicknesses of the two laminae significantly differ with thicknesses of 50–250 μm and 20–50 μm, respectively (Figure 5F). The OM is enriched in OCL.
7. DL + AL: DL and AL with thicknesses of up to 1 cm (Figure 5G).

Six laminated lithofacies can be identified based on the mineral composition: limestone, mixed fine-grained shale, silty limestone, dolomite shale, silty claystone, and gypsum shale. Among them, limestone, mixed fine-grained shale, and silty limestone are the dominant lithofacies and most widely distributed.

Massive Lithofacies

Massive Claystone and Siltstone—Massive claystone and siltstone (M1) are gray and blue-gray colored in the hand specimens (Figure 6A–C); they mainly developed in the lower Es4s interval, particularly at the 3471–3475-m depth of well NY1. The mineral composition mostly includes clay minerals (45%–56%), quartz and feldspar (10%–30%), and a small amount of calcite (less than 15%). Quartz and feldspar grains are disorganized and chaotic with no particular flow direction and comprise rare ostracod debris (Figure 6D, E). The lithofacies have low *TOC* (0.15%–0.69%) and a relatively higher vitrinite content than laminated shales (Table 1).

Massive Limestone and Silty Limestone—Massive limestone and silty limestone (M2) are dark gray and are mostly distributed in the 3320–3308-m interval with a thickness of 2 to 50 cm (Figure 6F–H), with small-scale scattered distributions in another interval in well NY1. Under microscopic inspection, micritic calcite is dominant (commonly accounting for 50% to 66%) and is mixed with clay minerals, microquartz, and feldspar (Figure 6I), and mineral grains are commonly chaotic and nondirective (Figure 6I, J). The lithofacies have a relatively higher *TOC* than M1, generally above 2%.

Massive dolomite—The hand specimens of the massive dolomite (M3) are light gray to gray, with a thickness of 10 to 50 cm (Figure 7A–C). The M3 has a dolomite content ranging from 29% to 61% (dominated by micritic dolomite) and clay and quartz ranging from 15% to 35%, which are relatively homogeneous and mixed with the micritic dolomite (Figure 7D, E). Moreover, euhedral dolomite is associated with anhydrite (Figure 7F, G). The lithofacies have a low *TOC* content (<1%), with OM associated with clay minerals.

Lenticular Laminae

Three types of lenticular laminae are present in the study area. Type I is typically convex in the middle, pointed at both edges, and comprises micritic calcite. The micritic calcite lens is relatively sparsely and directionally distributed among the clay minerals, with a size of approximately 50 to 200 μm along the long axis (Figure 8A1–A3). Furthermore, biological fragments are common. Type II is characterized by a flat and narrow intermittent lens; it is closely arranged along the long axis and has a typical lens size of approximately 500 μm, with some even up to 1000 μm (Figure 8B1–B3). A mixture of clay, quartz, and feldspar surrounds the lens. Type III is an irregularly shaped micritic calcite with a lens size ranging from 100 to 200 μm (Figure 8C1–C3). Type III mainly developed in the middle and lower Es4s interval.

DISCUSSION

Geochemical Characteristics and Analysis of Sedimentary Environment

The results of the Sr/Ba, S/*TOC*, and Th/U ratios and other geochemical elements signify that the Es4s–Es3x shale was deposited in a hypoxic saline lake (Figure 9). Due to the complexity of the factors influencing lake water such as salinity, oxidation reduction, and water depth with episodic high frequency (Figure 9), the results reflect the climate sensitivity of the lacustrine deposits. According to the geochemical characteristics, the Es4x–Es3x shale from well NY1 can be divided into five stages.

At the bottom of the Es4s–Es3x interval (3500–3481 m), the Na/Al ratio is high, the Mn content is low, the Mg/Ca, Fe/Mn, Fe/Co, Sr/Ba, and S/*TOC* ratios are relatively high, the salinity index Z value (calculated using carbon and oxygen isotopes) and K + Na contents are high, and the Al and Ti contents are slightly low, which suggests a cold and dry climate, making for shallow lake water. Due to low rainfall and significant evaporation, the lake water salinity was subject to strong stratification, which further exacerbated the strong reduction conditions in the water.

During the second stage (3481–3426 m), the Na/Al ratio decreased and the Mn content increased. Additionally, the Fe/Mn and Fe/Co ratios decreased, whereas the Sr/Ba and S/*TOC* ratios and the Z and K + Na contents remained at high values. Moreover, Al, Ti, pyrite and C_{org}/P were high, suggesting that the temperature began to recover and the climate gradually became warm and wet. Furthermore, the terrigenous input significantly increased, water depth increased, salinity continued to increase, and the degree of hypoxia of the water further increased.

In the third stage (3426–3362 m), Na/Al continued to decrease and the Mn content significantly increased. Moreover, the Mg/Ca, Fe/Mn, Sr/Ba, and S/*TOC* ratios and Z and K + Na all decreased, and Al, Ti, pyrite, and C_{org}/P slightly decreased. These characteristics suggest that the climate continued to become more warm and humid, resulting in a rising lake level, with the water depth reaching the maximum. The humid climate resulted in considerable rain and freshwater input, which decreased the water salinity.

In the fourth stage (3362–3318 m), the Fe/Mn and Fe/Co ratios slightly increased and the Sr/Ba and S/*TOC* ratios slightly decreased. The Al and Ti contents slightly increased. The climate was warmer but humidity and precipitation decreased, and the water depth decreased. Furthermore, the salinity slightly decreased, the waterbody reduction was relatively weak, and the input quantity of terrigenous debris increased.

Table 1. Composition, Thickness, Distribution, Sedimentary Characteristics and Sedimentary Conditions of Laminated Shale, Massive Mudstone and Lenticular Laminae Shale

Sedimentary Structure	Lithofacies	*TOC*, %	Laminae Composition	Thickness	Distribution	Sedimentary Characteristics	Sedimentary Conditions
Laminated shale	MCAL + OL + CL	2.4–4.7	MCAL	60–150 µm	Middle and upper Es4s–Es3x	MCAL have relatively low purity, with abundant microquartz and Na-feldspar.	High paleosalinity, low terrestrial material supply, and strong reducibility.
			CL	40–100 µm		OCL exhibits a scaly distribution with weak directivity.	
			OL	5–10 µm		OM is dispersed within the clay minerals.	
	SCAL + OCL	2.8–7.8	SCAL OCL	50–200 µm 10–400 µm	Bottom of Es3x, lower Es4s	No biological shell fragments. The sparry calcite is mainly granular with some Na-feldspar or quartz among the sparry calcite grains.	Rare terrigenous input.
	QFCL + OCL	2.1–3.0	QFCL OCL	40–80 µm 20–50 µm	Upper Es4s–Es3x	Complex mineral composition, including quartz, feldspar, clay minerals, and ostracum fragments. The particles in QFCL are disordered and poorly sorted. The OCL exhibit good lateral continuity	Relatively dry and cold climate, with low waterbody salinity and a stable supply of terrigenous debris.
	MCAL + QFCL	1.8–2.7	MCAL QFCL	60–150 µm 40–80 µm	Upper Es4s–Es3x	Rich in ostracod fragments.	Relatively strong hydrodynamic force and terrigenous inputs.
	DL + OCL	0.8–2.3	DL OCL	50–250 µm 20–50 µm	Lower Es4s–Es3x	Both DL and OCL exhibit good continuity with clear laminar boundaries.	Relatively dry climate, with a low input of terrigenous debris and high waterbody salinity.
	DL + AL	0.9–1.38	DL AL	Up to 1 cm Up to 1 cm	Bottom of the Es4s	Dolomite interbeded with anhydrite.	Relatively dry climate, with a low input of terrigenous debris and high waterbody salinity.

(*continued*)

Table 1. Continued

Sedimentary Structure	Lithofacies	*TOC*, %	Laminae Composition	Thickness	Distribution	Sedimentary Characteristics	Sedimentary Conditions
Massive mudstone	Massive claystone and siltstone	0.15–0.69	Clay: 45%–56% Quartz and feldspar: 10%–30%	2–50 cm	3471–3475 m	Relatively higher vitrinite content. Grains are disorganized and chaotic with no particular flow direction and comprise rare ostracod debris.	Low-salinity waterbody and strong terrestrial detrital input
	Massive limestone and massive silty limestone	1.7–2.9	Micritic calcite: 50%–66%	2–50 cm	3320–3308 m	Micritic calcite is dominant and mixed with clay minerals, microquartz, and feldspar. Mineral grains are commonly chaotic and nondirective.	Relatively warm climate, a lower terrigenous debris input, a relatively low salinity, a decrease in the hydrodynamic energy.
	Massive dolomite	0.8–1.5	Dolomite: 29%–61% Clay and quartz: 15%–35%	10–50 cm	Lower Es4s	Clay and quartz are relatively homogeneous and mixed with the micritic dolomite.	Dry and hot climate with strong evaporation.
Lenticular laminae	Type I	0.9–1.7	Calcite: 28%–36% Clay and quartz: 38%–62%	50–200 μm	Middle and upper Es4s interval	Convex in the middle, pointed at both edges with common biological fragments.	Relatively turbulent water body.
	Type II	1.2–2.2	Calcite: 41%–66% Clay and quartz: 19%–32%	500–1000 μm	Upper Es4s–Es3x	Flat and narrow intermittent lens with a mixture of clay, quartz, and feldspar surrounds the lens.	Sufficient terrigenous input.
	Type III: irregularly shaped micritic calcite	1.5–2.5	Calcite: 38%–55% Clay and quartz: 24%–41%	100–200 μm	Middle and lower Es4s–Es3x	Irregularly shaped micritic calcite lens with relative abundant benthic organisms.	Warm and humid climate, affected by different degrees of biodisturbances.

Abbreviations: AL = anhydrite laminae; CL = clay laminae; DL = dolomite laminae; Es4s = upper fourth member of Shahejie Formation; Es3x = lower third member of Shahejie Formation; MCAL = micritic calcite laminae; OCL = organic-rich clay laminae; OL = organic matter laminae; OM = organic matter; QFCL = quartz–feldspar–clay mixed laminae; SCAL = sparry calcite laminae; *TOC* = total organic carbon.

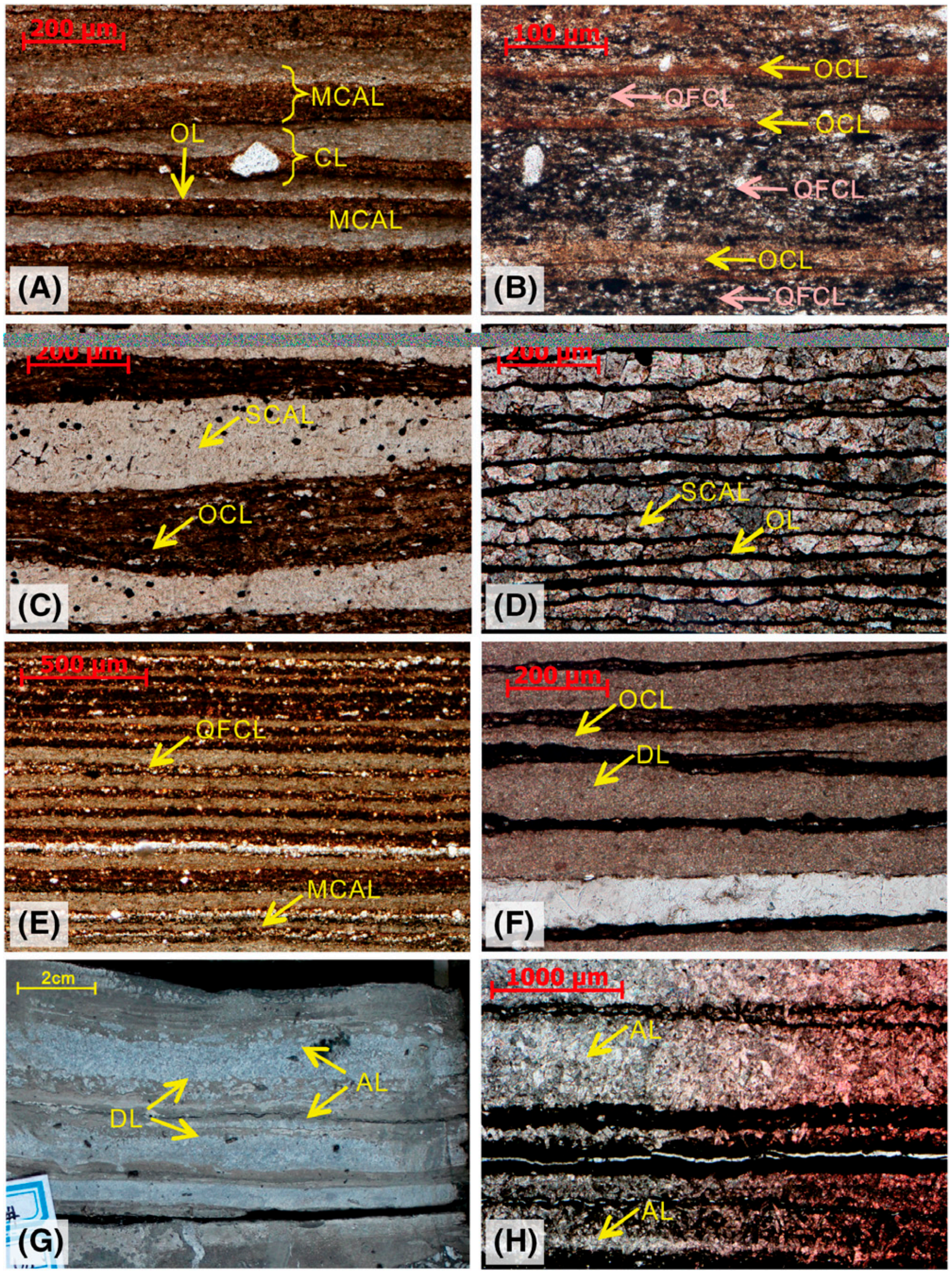

Figure 5. Lamina characteristics of the upper fourth member and lower third member of Shahejie Formation shale. (A) The lamina couplet (LC) comprising micritic calcite laminae (MCAL), organic matter laminae (OL), and clay laminae (CL), well NY1, 3420.90 m, cross-polarized light. (B) The LC comprising organic-rich clay laminae (OCL) and quartz–feldspar–clay mixed laminae (QFCL), well NY1, 3482.46 m, cross-polarized light. (C) The LC comprising sparry calcite laminae (SCAL) and OCL, well NY1, 3434.13 m, cross-polarized light. (D) The LC comprising SCAL and OL, well NY1, 3464.89 m, cross-polarized light. (E) The LC comprising QFCL and MCAL, well NY1, 3410.86 m, cross-polarized light. (F) The LC comprising dolomite laminae (DL) and OCL, well NY1, 3466.15 m, cross-polarized light. (G) The LC comprising DL and anhydrite laminae (AL), well NY1, 3496.68 m. (H) AL, well NY1, 3488.23 m, cross-polarized light.

In the fifth stage (3318–3295 m), the Na/Al ratio slightly increased, and the Mn content significantly decreased. The Mg/Ca, Fe/Mn, and Fe/Co ratios increased, the Z content slightly increased, and the Al, Ti, and pyrite content and the C_{org}/P ratio increased. This suggests that the temperature and humidity continued to decrease relative to the previous stage. Additionally, the lake level was relatively low, and salinity and water reduction slightly increased.

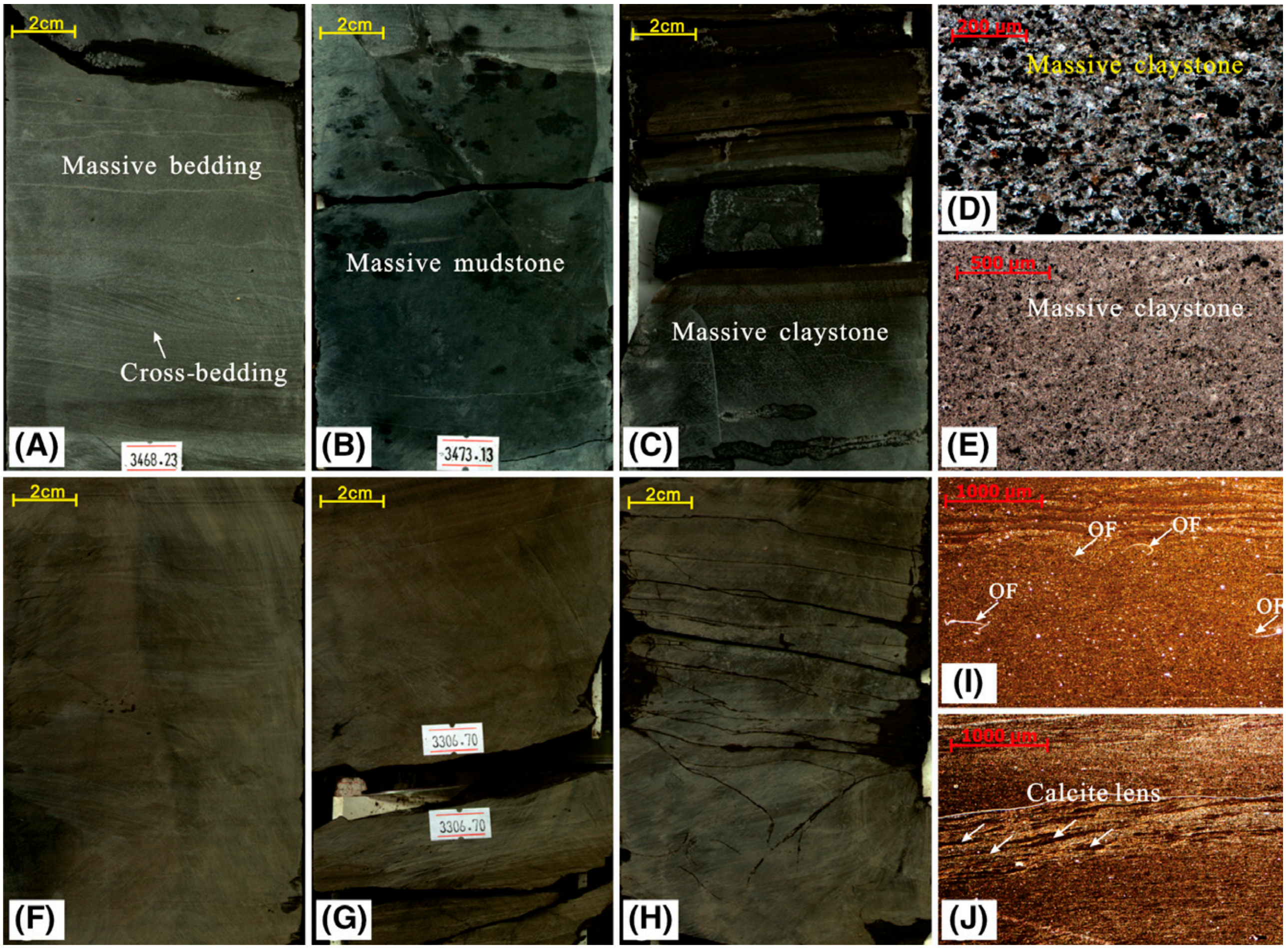

Figure 6. Characteristics of massive silty claystone (A–E) and massive limestone (F–J). (A) Siltstone with cross-bedding and massive bedding, well NY1, 3468.23 m. (B) Massive silty claystone, well NY1, 3473.1 m. (C) Massive claystone, well NY1, 3367.5 m. (D) Thin-section image of the massive claystone, well NY1, 3472.99 m, cross-polarized light. (E) Thin-section image of the massive claystone, well NY1, 3471.68 m. (F) Massive limestone, well NY1, 3305.95 m. (G) Massive limestone, well NY1, 3306.7 m. (H) Massive limestone, well NY1, 3313.4 m. (I) Massive silty limestone with ostracod fragments (OF), well NY1, 3303.31 m. (J) Massive limestone, well NY1, 3314.3 m.

Formation of Different Shales with Different Sedimentary Structures

Laminated Shale with Different LCs

LC-I—In LC-I, MCAL are 20–120 μm thick, with a usual thickness of 100 μm (Figure 10A, B). The MCAL have relatively low purity, with abundant microquartz and Na-feldspar (Figure 10C). The OCL are approximately 10–35 μm thick, which are thinner than MCAL, and the minerals are well sorted in OCL, exhibiting a scaly distribution with weak directivity. The OCL comprise few quartz and feldspar grains with a grain size of approximately 1 to 10 μm, and OM is evenly dispersed within the clay minerals. Elemental analysis suggests that light and dark laminae are commonly in abrupt contact, with clear laminar boundaries (Figure 11A). As observed by FE-SEM, electron probe microanalysis line scanning suggests that individual points have high Si, Al, and K contents and that Sr and B contents are slightly higher overall (Figure 11A).

The MCAL + OL + CL (Figure 12) reflect the development in a sedimentary environment with high paleosalinity, low terrestrial material supply, and strong reducibility. The characteristics of these LCs are consistent with the mixed calcareous organic (mixed) varve mud recorded from Holocene lakes (Figure 10D). Plankton blooms changed the pH value of water through photosynthesis, promoting calcite precipitation in a biochemical manner, which mainly occurs in warm and humid spring and summer seasons. As the climate became colder,

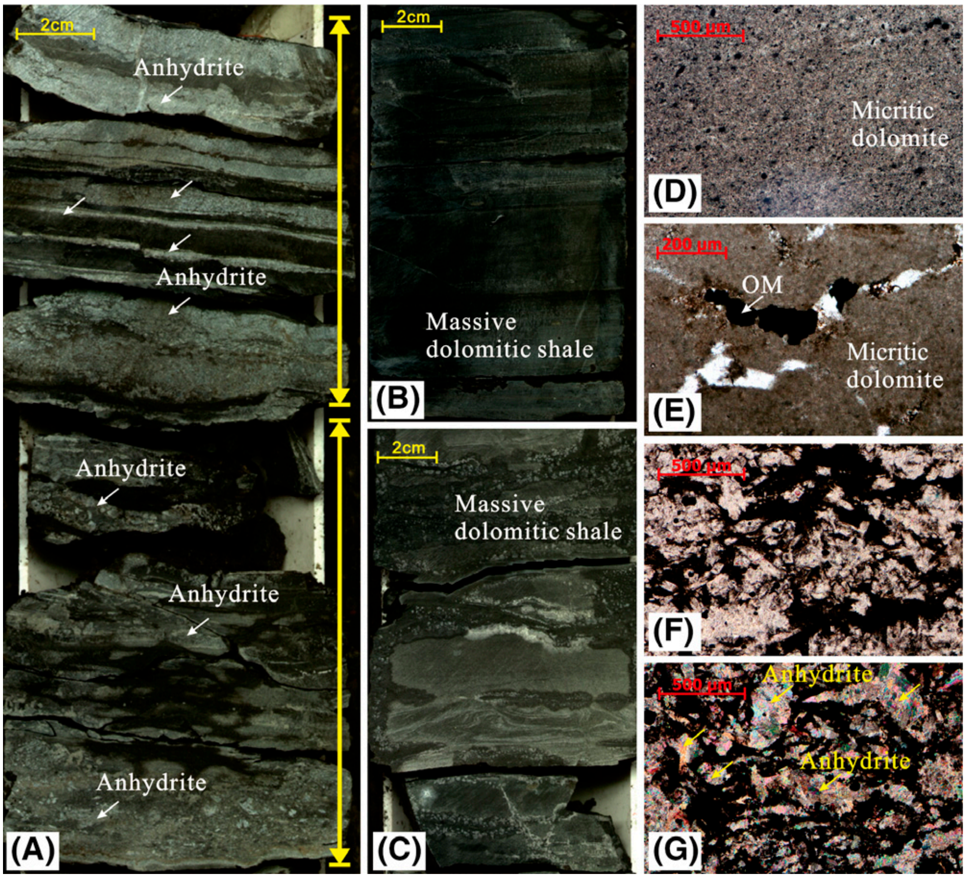

Figure 7. Characteristics of massive dolomitic shale. (A) Massive dolomitic shale with anhydrite, well NY1, 3497.8–3498.0 m. (B) Massive dolomitic shale, well NY1, 3468.5 m. (C) Massive dolomitic shale, well NY1, 3496.3 m. (D) Massive dolomitic shale with micritic dolomite, well NY1, 3471.68 m. (E) Massive dolomitic shale with micritic dolomite, well NY1, 3475.9 m. (F) Anhydrite associated with massive dolomitic shale, well NY1, 3498.30 m. (G) Anhydrite associated with massive dolomitic shale, well NY1, 3496.43 m. OM = organic matter.

numerous organisms died, but some survived through oxidation and were preserved, forming OL. Because a large number of organisms died, the carbonate precipitation decreased due to the lack of biological effects and terrigenous precipitation increased, yielding carbonate- and organic-poor and clay-rich laminae, which always occur in the winter (Figure 10D).

LC-II—The QFCL are approximately 30–50 μm thick (Figure 13) with a maximum thickness of 500 μm, and have a complex mineral composition, including quartz, feldspar, clay minerals, and ostracum fragments (Figure 13C, D). The particles in QFCL are disordered and poorly sorted. The content of terrigenous clastic components is high. The OCL exhibit good lateral continuity, with a lamina thickness of approximately 10 μm, which is less than that of QFCL. Sparry calcite and diagenetic quartz grains are dispersed along the laminar boundaries (Figure 13C), with a grain size of 20 to 50 μm, whereas OM is mostly combined with clay minerals to form an OM–clay complex. Electron probe microanalysis line scanning suggests that OCL and QFCL are in gradual contact with each other, with unclear laminar boundaries. The Si, Al, and K contents do not significantly vary in the different laminae, and the Sr and B contents are relatively low overall (Figure 11B).

This LC was well developed for 3384 to 3358 m and 3303 to 3295 m and was deposited under a relatively dry and cold climate, with low waterbody salinity and a stable supply of terrigenous debris (Figure 9), which led to the overall dominance of laminated clay minerals. A certain amount of material exchange also occurred between laminated units, and the difference in mineral composition is not significant (Figure 13A, B). Seasonal blooms and culls of organisms allowed the silt mixture to be suspended and deposited in the warm spring and

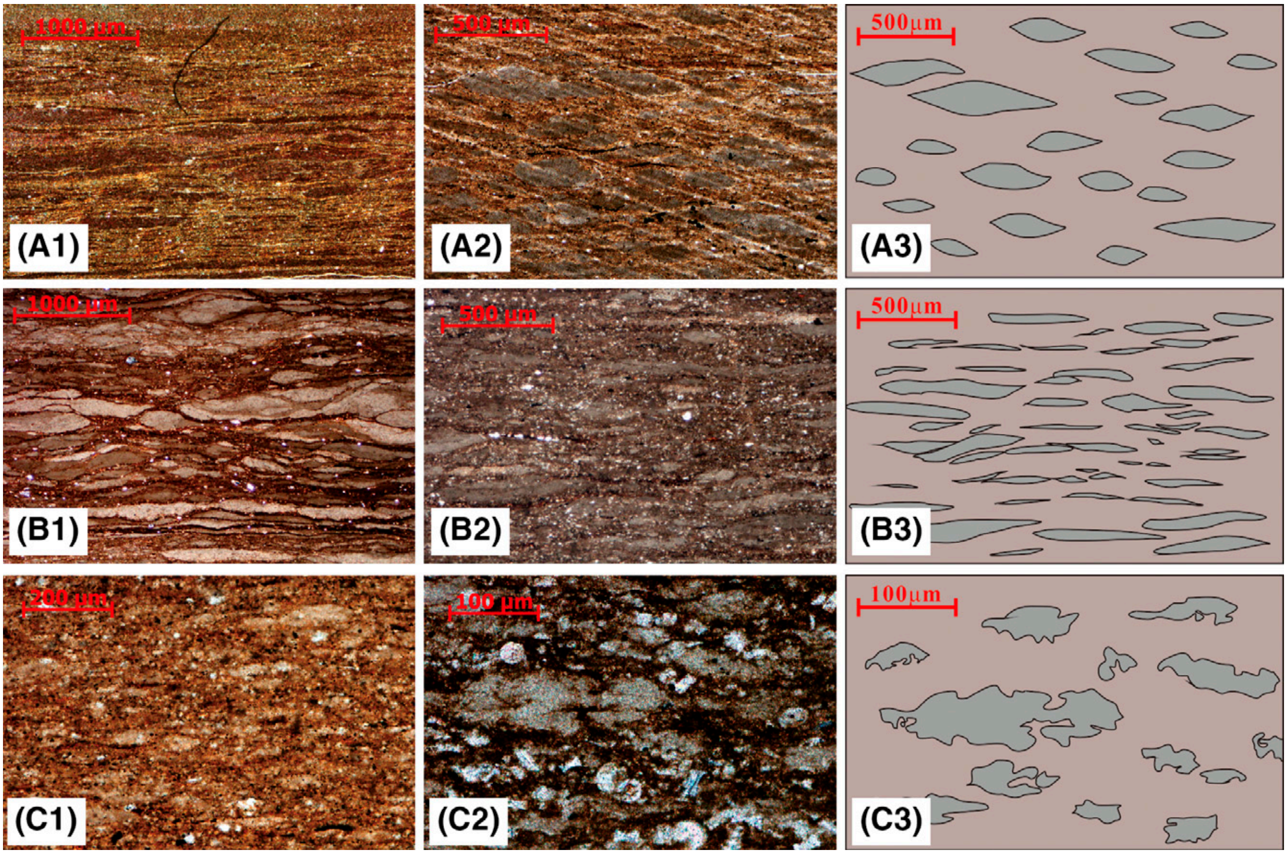

Figure 8. Characteristics of lenticular laminae. (A1–A3) Type I lenticular laminae distributed sparsely and directionally among the clay minerals. (A1) Type I micritic calcite lens, well NY1, 3303.57 m. (A2) Type I micritic calcite lens, well NY1, 3404.7 m. (A3) Schematic of (A2). (B1–B3) Type II lenticular laminae with a flat and narrow intermittent lens. (B1) Type II micritic calcite lens, well NY1, 3347.56 m. (B2) Type II micritic calcite lens, well NY1, 3368.83 m. (B3) Schematic of (B2). (C1–C3) Type III lenticular laminae with irregularly shaped micritic calcite lens. (C1) Type III micritic calcite lens, well NY1, 3304.62 m. (C2) Type III micritic calcite lens, well LY1, 3833.92 m. (C3) Schematic of C2.

summer, whereas in the cold autumn and winter, the remains of organisms and clay minerals precipitated together, yielding OCL. Due to the low salinity and relatively weak reducibility of the waterbody and the poor conditions of preservation for OM, the *TOC* of this LC is relatively low.

LC-III and LC-IV—The SCAL + OCL couplet is similar to the SCAL + OL couplet. The laminae units of both LCs have pure components with clear laminar boundaries (Figures 12, 14).

The LC-III has a rare terrigenous input and no biological shell fragments, with thick SCAL and thin OCL (Figure 14A, B). The sparry calcite is mainly granular, with a grain size of 10 to 100 µm; SCAL have a pure component (Figure 14C), with some Na-feldspar or quartz among the sparry calcite grains (Figure 14D). The electron probe microanalysis shows that SCAL have high purity with a Ca content of approximately 75% (Figure 15A). Generally, the laminae are characterized by clear and continuous laminar boundaries. The OCL are mainly thick (20–50 µm) and have high Si, Al, and K content, with rare small-sized quartz and feldspar (Figures 14C, D; 15A). Moreover, the sparry calcite has a higher Sr content than MCAL, as shown in Figure 15A and B. The elemental line scans suggest an abrupt contact between different laminae (Figure 15A).

LC-V—In LC-V (Figure 12C), the QFCL units are rich with ostracod fragments, suggesting the influence of relatively strong hydrodynamic forces and terrigenous inputs, which resulted in the modification of the carbonate laminae (Figure 16A, B).

The MCAL are approximately 50–100 µm thick and have high purity with a Ca content of

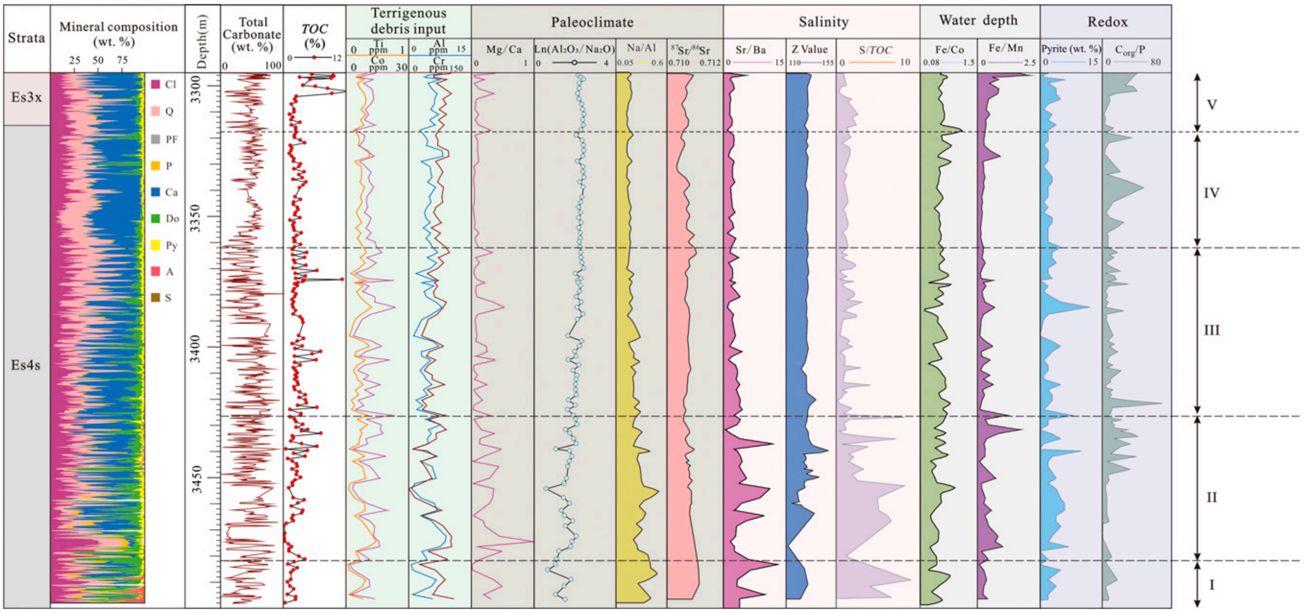

Figure 9. Geochemistry and main mineral composition of upper fourth member and lower third member of Shahejie Formation shale in well NY1. A = anhydrite; Ca = calcite; Cl = clay; C_{org}/P = organic carbon/phosphorus ratio; Do = dolomite; P = plagioclase; PF = potassium feldspar; Py = pyrite; Q = quartz; S = siderite; Z = salinity index Z value (calculated using carbon and oxygen isotopes).

approximately 65% (Figure 15C). Generally, the laminae are characterized by clear and continuous laminar boundaries and few exhibit poor continuity (Figure 16C, D). The OCL are mainly 20–50 μm thick and have high Si, Al, and K contents, with some small grains (quartz and feldspar) aligned along the long axis of the grains (Figure 15C). The differences between the different laminae suggest that light-colored laminae have a relatively high B content, whereas dark-colored laminae have high Si, Al, and K contents. The line scan curves of the elements suggest the gradual-to-abrupt contact of different laminae (Figure 15C).

Vertically, such laminae mainly develop in strata with increased continental transport, relatively small OM content, and decreased reducibility (Figure 9). The continuous fine laminae contain OL without biological shell fragments or silty sand, which is consistent with the analysis of the sedimentary environment. The well-developed laminae indicate that they comprise deep water, strong water stratification, and relatively small land-based input (Figure 9). The continuous fine lamination (clay + felsic clastic laminae) has OM mixed with clay minerals and quartz particles. Analysis of the sedimentary environment indicates that it developed during a large land-based input interval (Figure 9).

LC-VI and LC-VII—The LC-VI is mainly present in the lower Es4s–Es3x interval. The micritic DL are mainly relatively thick (50–400 μm), whereas OCL are 10–50 μm thick. Generally, both DL and OCL exhibit good continuity with clear laminar boundaries (Figure 5F). The LC-VII is mainly present at the bottom of the Es4s–Es3x interval (Figure 9) with thick laminae of approximately 0.1 to 1 cm (Figure 5G). Based on the sedimentary environment shown in Figure 9, LC-VI and LC-VII mainly developed in a relatively dry climate, with a low input of terrigenous debris and high waterbody salinity.

LCs within Different Lithofacies

In the laminated limestone, LC-I, LC-III, LC-IV, and LC-V are well developed. The LC-II has clear laminar boundaries, a high *TOC* content, and strong lake waterbody reducibility. The laminar boundaries in LC-V may or may not be clear, wherein lithofacies with clear laminar boundaries signify drier climate, higher salinity, and less terrestrial debris input than lithofacies with intermittent laminar boundaries. Additionally, the results suggest that the water depth of LC-I exceeds that of LC-V, as shown in Figure 17B.

In the mixed fine-grained sedimentary rocks (FGSRs), LC-V and LC-I have clear or fuzzy continuous laminar boundaries. The results signify that the

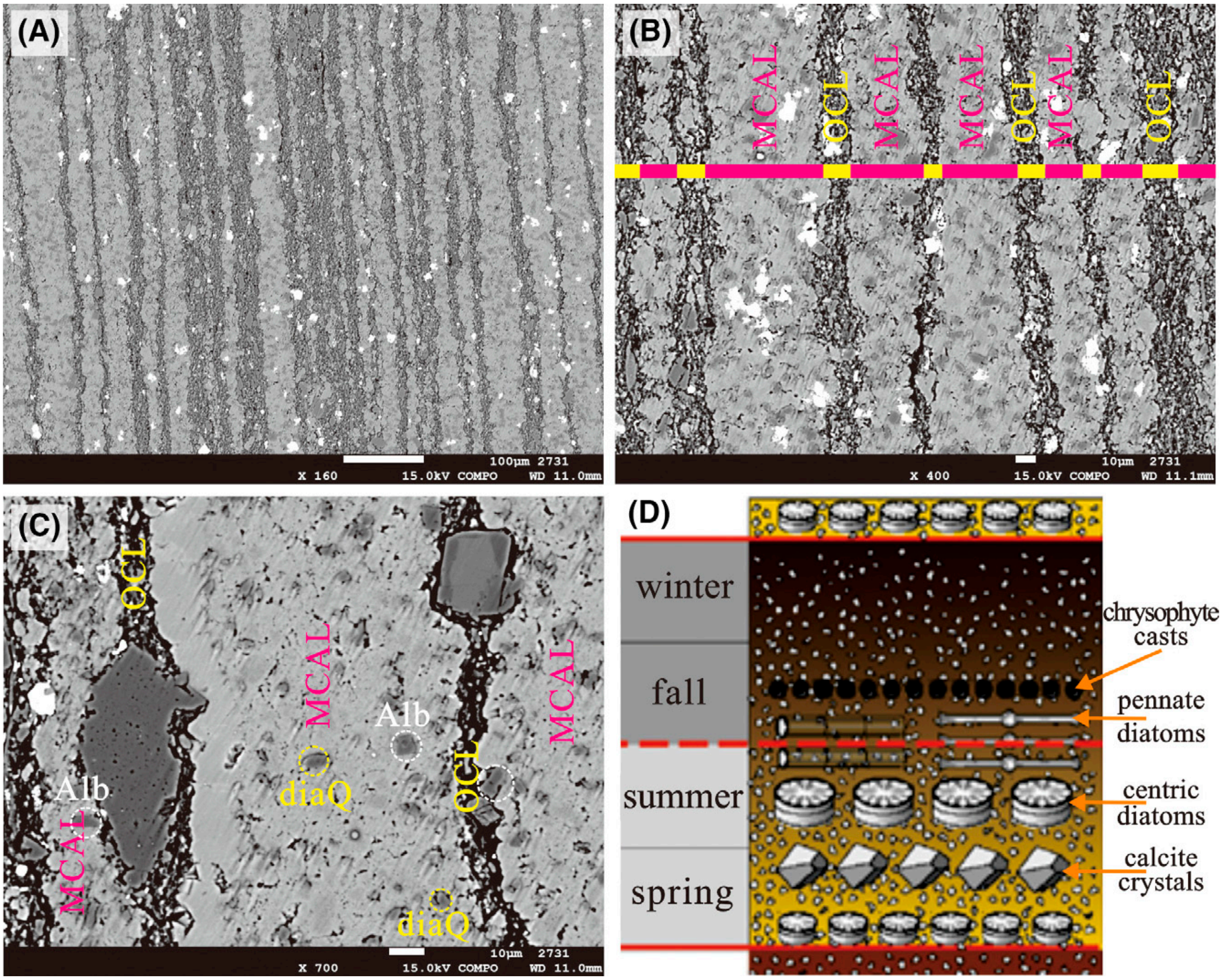

Figure 10. Characteristics of micritic calcite laminae (MCAL) + organic-rich clay laminae (OCL). (A, B) Scanning electron microscopy photos display the light and thick MCAL (20–120 μm) and the dark and thin OCL (10–35 μm), well NY1, 3445.75 m. (C) The MCAL with abundant micro diagenetic quartz (diaQ) and albite (Alb), size approximately 1–10 μm. (D) Simplified models for depositions of a calcareous organic (mixed) varve (modified from Zolitschka et al., 2015).

mixed FGSRs were deposited under a relatively strong terrigenous input environment (Figure 17A), regardless of the type of paired laminae, and the main difference between the different paired laminae is the paleoclimate. As shown in Figure 8C, LC-V and LC-III generally developed in a warm and humid climate, whereas LC-VI developed in a relatively mild climate with high salinity. The LC-V has intermittent laminae with relatively deep water and low terrigenous input but high oxygen content, suggesting that the intermittent laminae may be caused by bioturbation. In LC-III, the selected lithofacies are mainly differentiated by the *TOC* content, and those with higher *TOC* content have higher pyrite content and Ni/Co ratio, suggesting that reducibility is essential and conducive for OM preservation. Few data points were obtained for LC-VI, and diversity is not obvious. The LC-V mainly comprises silty limestone with continuous fuzzy or intermittent laminae, wherein the intermittent laminae reflect a drier climate, shallower lake water, and more terrigenous input than continuous laminae.

Massive Lithofacies and Deposition

M1—The debris grains (mainly quartz) in the massive claystone are disorganized and chaotic with no particular flow direction and comprise rare ostracod debris (Figure 6D, E). The lithofacies have a lower *TOC* content (0.15%–0.69%) and a relatively higher vitrinite content than laminated shales. The sequences of

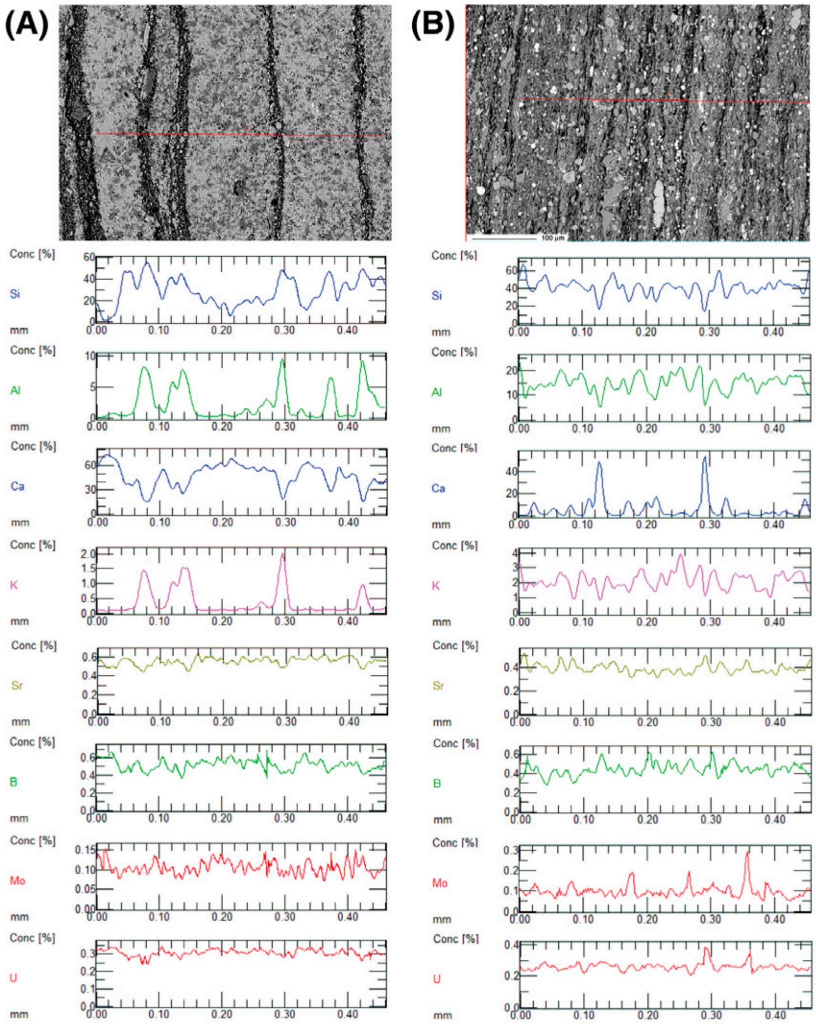

Figure 11. Elemental analysis by electron probe microanalysis line scan of micritic calcite laminae + organic-rich clay laminae (OCL) (A), and quartz–feldspar–clay mixed laminae + OCL (B). The red lines refer the position of the electronic probe line scan. Conc = concentrations.

lithofacies in massive mudstone from bottom to top are (1) siltstones, massive claystone, and laminated shale; (2) siltstones and massive mudstones; and (3) mudstones and laminated mudstones; a single sequence of lithofacies has a thickness of 0.05 to 0.55 m (Figure 17A). Every sequence of lithofacies has abrupt contact interfaces with underlying laminated shales and gradual contact interfaces in the interior. Thus, this siltstone and the associated organic-poor massive mudstone lithofacies are interpreted as fine-grained turbidites. High silt-grain content, low Sr/Ba and S/*TOC* ratios, and the Z value suggest a low-salinity waterbody and strong terrestrial detrital input (Figure 18A), which is mainly from a shallow lake, such as delta sediments. Furthermore, the debris-flow currents transported abundant O_2 to the lake bottom, causing OM oxidation. Moreover, due to the high deposition-rate dilution, M1 has a low *TOC* content.

M2—Vertically, the massive limestone is associated with MCAL-developed shale, such as laminated silty limestone or laminated mixed shales, but is rarely associated with laminated limestone (Figure 18B). Massive limestone has a grain size similar to that of these laminated shales, with abrupt contact interfaces with laminated shales. As shown in Figure 17B, discontinuous laminae developed at the bottom of the massive lithofacies, which are covered by continuous MCAL at the top.

A relatively low Z value and low Na/Al and Mg/Ca ratios suggest that M2 was deposited under a relatively warm climate (Figure 18B). The Sr/Ba ratio

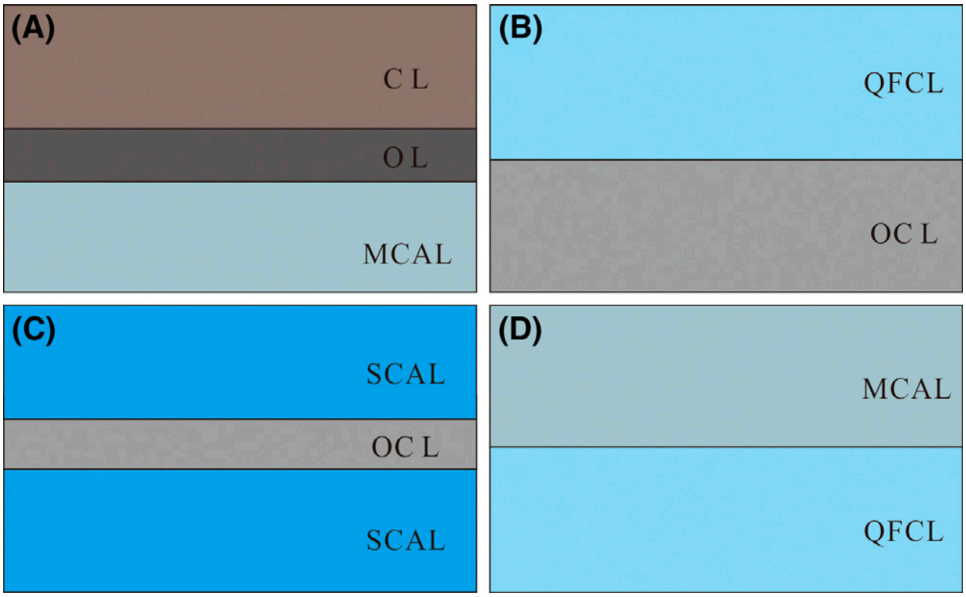

Figure 12. Schematic diagram of typical lamina couplets: micritic calcite laminae (MCAL) + organic matter laminae (OL) + clay laminae (CL) (A), organic-rich clay laminae (OCL) and quartz–feldspar–clay mixed laminae (QFCL) (B), sparry calcite laminae (SCAL) + OCL (C), and MCAL + QFCL (D).

is generally about 1.0, which is low for the entire Es4s–Es3x shale (Figure 9), suggesting a relatively low salinity. The Ti and Al contents suggest a lower terrigenous debris input for M2 than that for M1 and M3 (Figure 18). Geochemical elemental analysis and sedimentary characteristics suggest that M2 may stem from a fine-grained turbidity current, whose sediments mainly arise from the resuspension of bottom sediments mixed with quartz, clay, and feldspar, as well as rapid subsidence from massive limestone or silty limestone. A decrease in the hydrodynamic energy led to deposition under the suspension of laminae limestone and silty limestone comprising MCAL and OCL. The M2 at the bottom and the laminated lithofacies at the top represent a turbidity deposition event. In contrast to M1, the sediments in M2 are mainly suspension sediments resuspended in the semideep or deep lake rather than coarse debris from relatively shallow lakes. Geochemical analysis shows that OM is less oxidized in M2 than in M1 due to lack of oxygen input, and thus, a higher *TOC* content is preserved.

M3—The M3 is mainly present in the lower Es4s interval and is vertically deposited with dolomitic laminated shale and anhydrite laminated shale (Figure 17C). Geochemical elemental analysis and petrology characteristics suggest that the lithofacies were deposited in a dry and hot climate with strong evaporation (Figure 18C). Under strong evaporation, the dolomite precipitation rate was fast, and consequently, a thick massive bedding formed in a short time (Liang et al., 2018). Due to the decreasing temperature, reduced evaporation, and relatively low deposition rate, dolomitic laminae paired with OCL or AL formed.

Lenticular Laminae

The micritic calcite lens in type I is accompanied by biological fragments that are similar in size (50–200 μm) and the micritic calcite lens is distributed relatively sparsely and directionally (Figures 8A1–20A3). Type I mainly developed in the middle and upper parts of Es4s interval, the deposition conditions during which were characterized by a relatively turbulent water body. Under the relatively strong hydrodynamics, the deposited MCAL may break down and resuspend, yielding the lenticular feature.

Type II is characterized by a flat and narrow intermittent lens, with a lens size of generally approximately 500 μm, and a mixture of clay, quartz, and feldspar surrounds the lens. Type II mainly developed in the interval with sufficient terrigenous input and deep water. This is because a muddy deposit that was rich in water was eroded, transported, and deposited along the bed, and relatively strong compaction

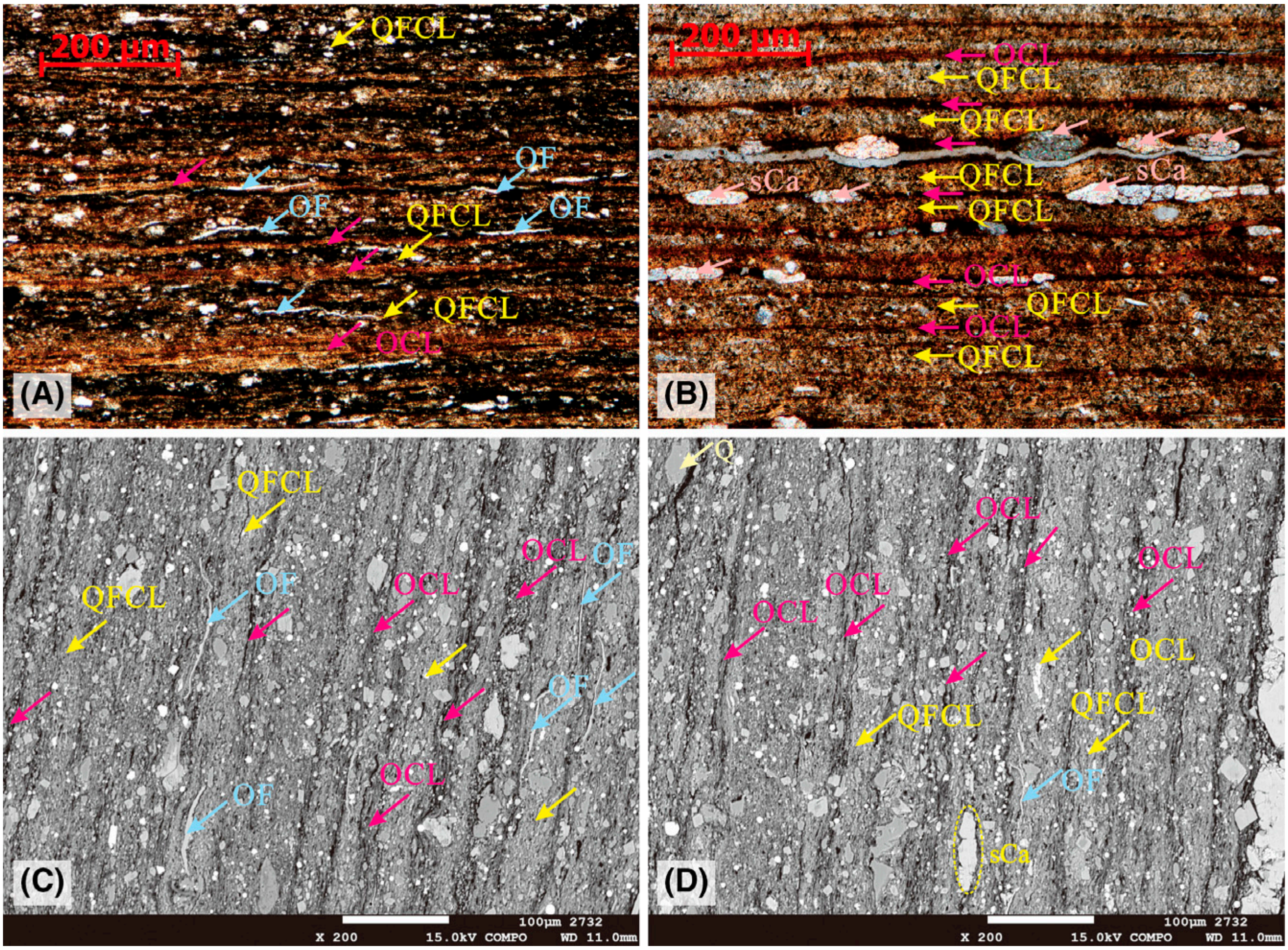

Figure 13. Characteristics of organic-rich clay laminae (OCL) and quartz–feldspar–clay mixed laminae (QFCL). (A, B) Thin-section images. (A) Ostracod fragments (OF) occur in QFCL, well NY1, 3480.5 m, thin-section image. (B) Lenticular sparry calcite (sCa) developed in the laminae interfaces, well LY1, 3662.73 m. (C, D) Field-emission scanning electron microscopy images. The OFs and quartz (Q) grains in QFCL and sCa in the laminae interfaces, well NY1, depth of 3315.75 m.

occurred during the burial stage (Schieber et al., 2010).

The irregularly shaped micritic calcite in type III mainly developed in the middle and lower Es4s interval. During this period, the climate was warm and humid with relatively abundant benthic organisms. Therefore, we assume that the formation of such lenses may be affected by different degrees of biodisturbances.

Depositional Model

The depositional model was established to determine the origin of different shales with laminated, massive, and lenticular beddings. In the model, the development of the laminae unit sets is controlled by the hydrological conditions, paleoclimate, terrigenous supply, and deposition process. The "key point" is the halocline location in the lake, which is controlled by the lower limit of the terrigenous material because terrigenous materials desalinate the lake water in the area that they reach. Thus, the difference between the upper and lower halocline influences the composition and interface of the lamina units. Furthermore, the halocline is controlled by the balance of the water depth and terrigenous input.

At the upper halocline, the lenticular laminae are discontinuous and there are no well-developed calcareous laminae (Figure 19). These laminae are influenced by terrigenous materials and strong hydrodynamic conditions (Figure 19). Compared to discontinuous MCAL + QFCL, the noncalcareous laminae signify the influence of a terrigenous source and a strong hydrodynamic force. In the areas with

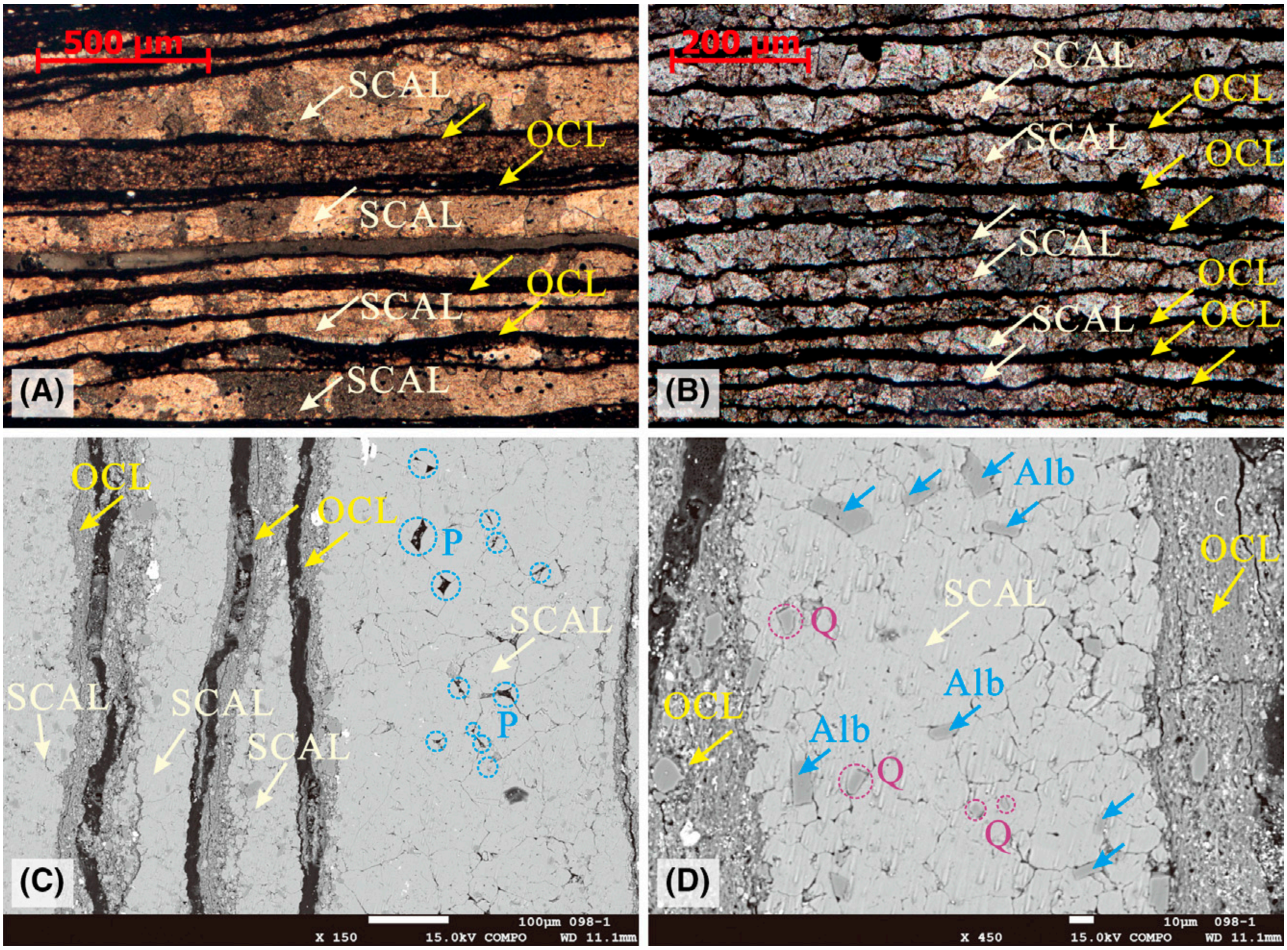

Figure 14. Characteristics of sparry calcite laminae (SCAL) + organic-rich clay laminae (OCL) or organic matter laminae. (A, B) Thin-section images. (A) Thick SCAL and thin OCL, well NY1, 3437.13 m. (B) Thick SCAL and thin OCL, well NY1, 3464.89 m. (C, D) Field-emission scanning electron microscopy images. (C) Interparticle pores (P) in SCAL, with a size of 10 to 50 μm, well NY1, 3460.23 m. (D) Dia-quartz (Q) and albite (Alb) in SCAL, with a size of 5 to 20 μm, well NY1, 3460.23 m.

terrigenous materials, the poor laminae continuity, discontinuous or lenticular laminae, and the fuzzy laminar boundaries reflect the relatively complex sediment supply (Figure 8). Moreover, OM is commonly scattered and mixed with clay minerals and calcite, with some terrestrial OM. Below the halocline, terrigenous particles are sporadically present, whereas carbonate minerals and clays are abundantly present in the laminae. Clay minerals are transported to deep waters in the form of flocculation or suspension. Furthermore, the laminae exhibit good continuity with clear laminar boundaries, and the enriched OM forms thin continuous laminae mixed with various inorganic minerals, corresponding to the laminae in the upper halocline (Figure 19). Generally, the *T*OC content is high, including mainly plankton alga with rare terrestrial OM. The laminae continuity and the clarity of the laminar boundaries reflect the stable, quiet, and deep-water environment and the distinct differences in the sediment supply in the deep lake, which may be caused by the seasonal variations of the sediment supply. At the key point, different genetic components form, and the key point fluctuates with the water depth and terrigenous input. Therefore, the laminar composition of sediments gradually transforms with the blurred laminar boundaries.

In the first stage below the halocline, the MCAL + OL + CL is dominant. In this stage, the tiny carbonate particles produced via biochemical action may not be sufficient for overcoming the buoyancy and precipitate; then, they are adsorbed on clay minerals for forming larger assembled particles and then precipitate. The relevant evidence includes microcalcite-clay assembled particles (1–3 μm; Figure 10C, D)

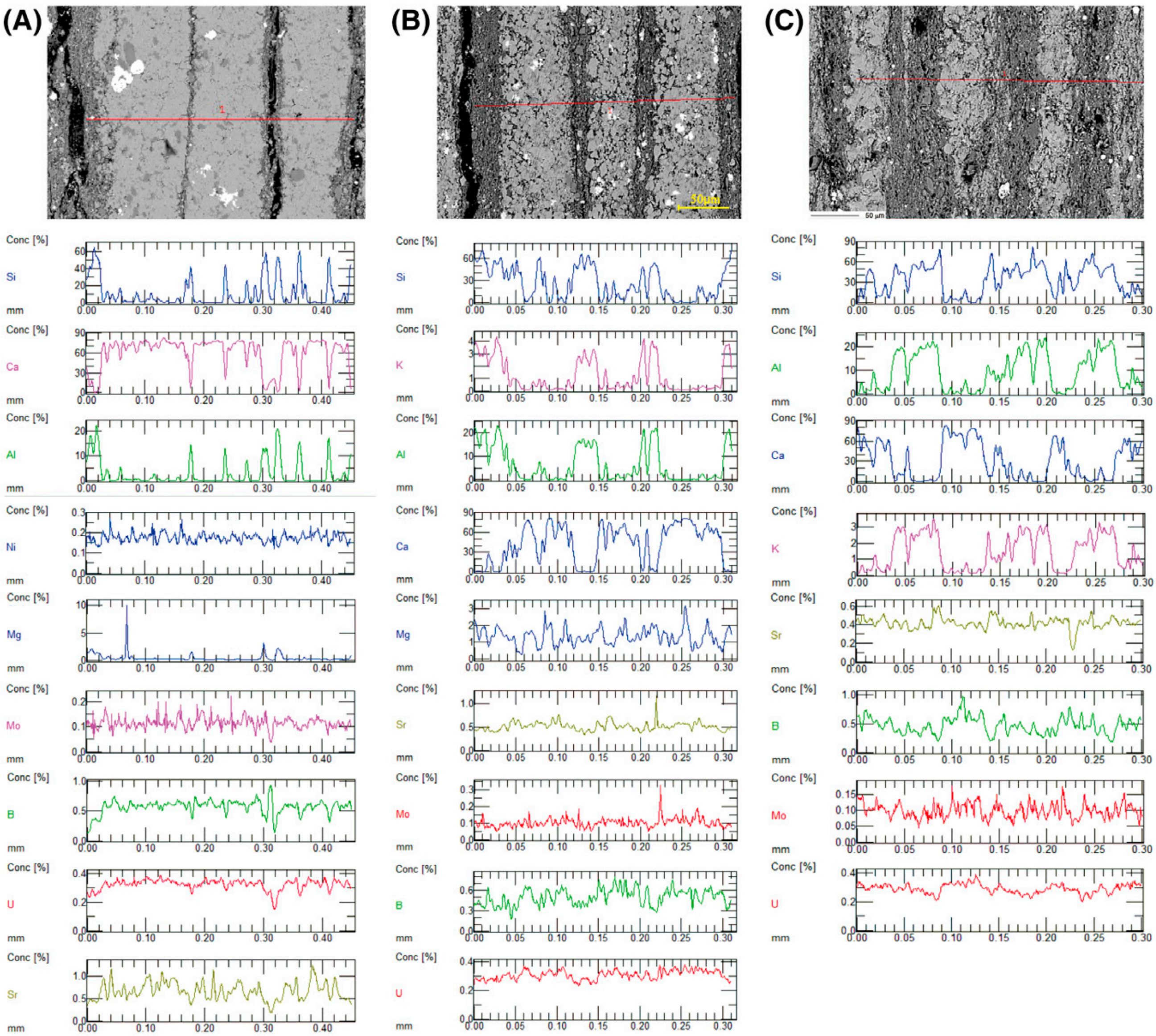

Figure 15. Electron probe microanalysis line scan of (A) sparry calcite laminae + organic-rich clay laminae (OCL), (B) micritic calcite laminae (MCAL) + OCL, and (C) MCAL + quartz–feldspar–clay mixed lamina. The red lines denote the position of the electronic probe line scan. Conc = concentration.

and far greater Ca content in clay than normal, which reaches 20%–30% in the clay-rich laminae, as detected in the electron probe microanalysis (Figure 11A).

In the deeper areas, the clay mineral supply decreases because of the increase in distance and consumption in the previous stage; thus, SCAL + OL is dominant (Figure 14). The key-point position fluctuates with time and is influenced by changes in the continental supply, water depth, climate, and other factors in the sedimentary conditions, which result in rapid and frequent vertical changes of the laminar assemblage in shale. As mentioned above, the key-point position is controlled by both the terrigenous input and water depth. This denotes that the halocline position does not necessarily move upward when the water depth increases. This is because as the water depth increases, the increasing terrigenous input carries more fresh water and moves further to the deeper point. Therefore, the halocline vertical change depends on the dynamic balance between the water depth and terrigenous input; differences in lamina units and OM depend on the dynamic balance between the water depth and terrigenous input (Figure 19).

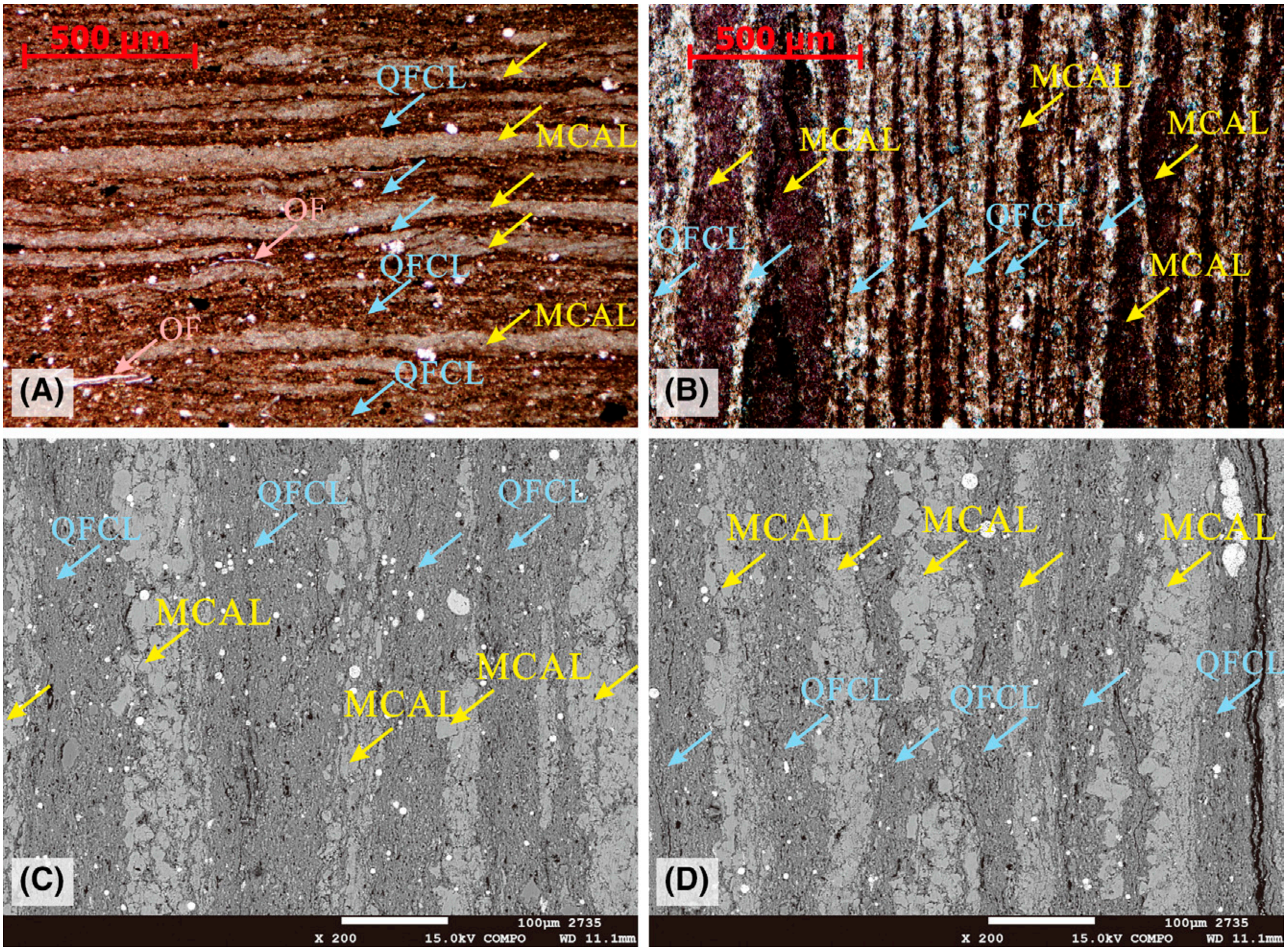

Figure 16. Characteristics of micritic calcite laminae (MCAL) + quartz–feldspar–clay mixed laminae (QFCL). (A, B) Thin-section images. (A) Ostracod fragments (OF) are common in the lamina couplet, well NY1, 3443.55 m. (B) Frequent interbedding of MCAL with QFCL, well LY1, 3680.21 m. (C, D) Field-emission scanning electron microscopy images show the variable thickness of MCAL and QFCL, well NY1, 3317.52 m.

Significance for Paleoclimate Reconstruction Using Lacustrine Sedimentary Records

Geomorphology, the chemical properties of bedrocks, insolation amount, precipitation, and evaporation all affect the formation of lacustrine varves (Zolitschka and Enters, 2009; Ojala et al., 2012; Ebert and Trauth, 2015). The precipitation of sediments was influenced by seasonal variations in sediment supply, which produced a variety of LCs (Zolitschka et al., 2000; Wittkop et al., 2009; Ebert and Trauth, 2015; Schimmelmann et al., 2016). In pre-Quaternary geological records, as reported herein, the laminae components and occurrence are controlled by the paleohydrological conditions and terrigenous sediment input in the ancient lakes. These controlling factors are closely related to the paleoclimate, or more precisely, the multiscale periodic climate changes controlling the evaporation of the lake water and rainfall. The salinization of the lake water body is a necessary condition for the formation and preservation of seasonal laminae. As mentioned herein, the laminae types with better stratification mostly developed in intervals with relatively higher salinity.

Astronomical analysis suggests that the depositional rate of the Es4s interval is 95 μm/yr (Shi et al., 2018). However, the average thickness of carbonate laminae and CL is less than that indicated by the data from laminae records (Figure 5). This further indicates that these shales are not the result of stable deposition nor are they the result of seasonal lamination. Massive shales and intermittent laminates also support this result. Although laminae are generally

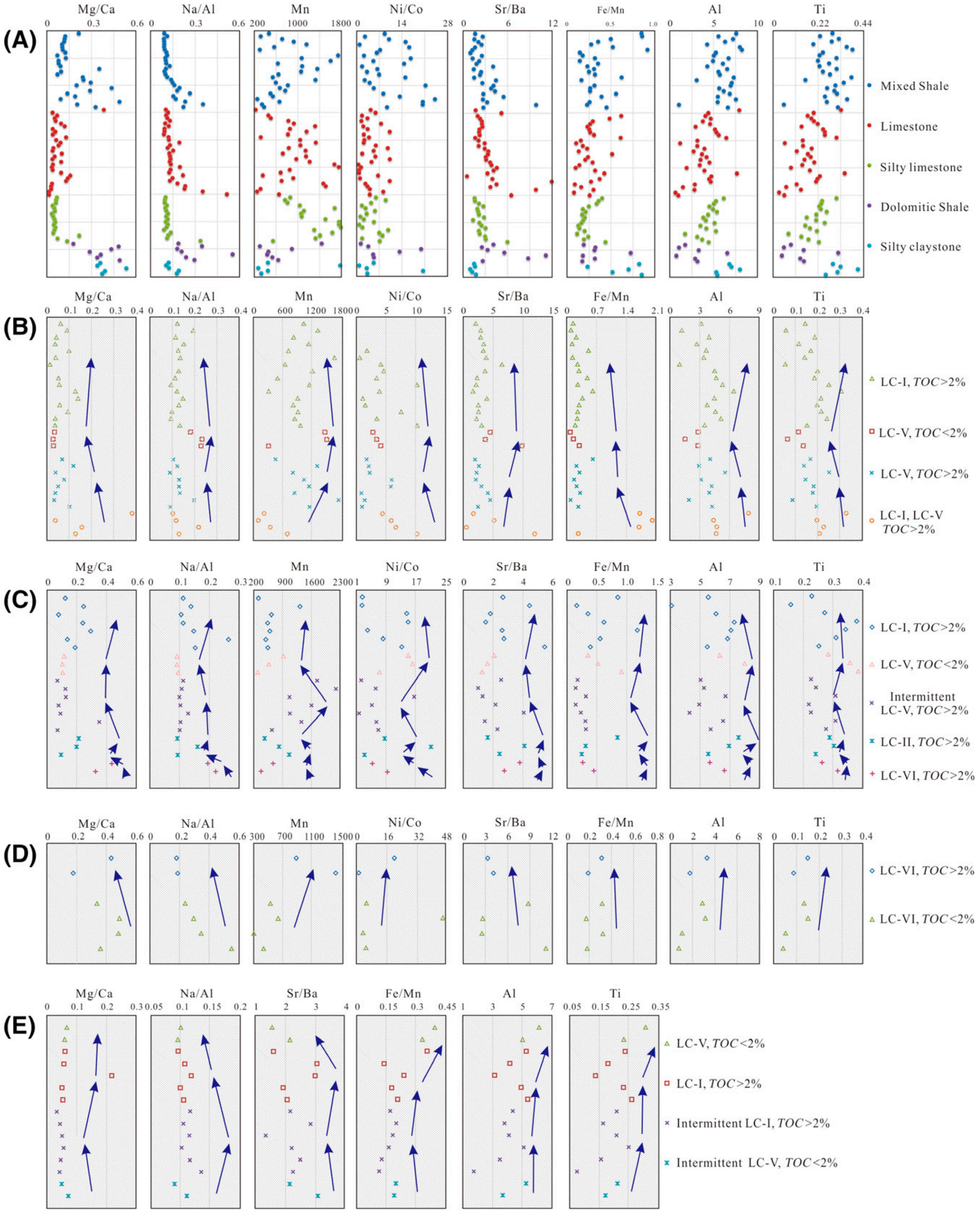

Figure 17. Comparison of the characteristics of the lamina couplets (LC) in different lithofacies types. Sedimentary geochemistry correlation of different lithofacies (A). Sedimentary geochemistry correlation of different paired laminae in limestone (B), mixed shale (C), dolomitic shale (D), and silty limestone (E). The blue arrows indicate the trend. *TOC* = total organic carbon.

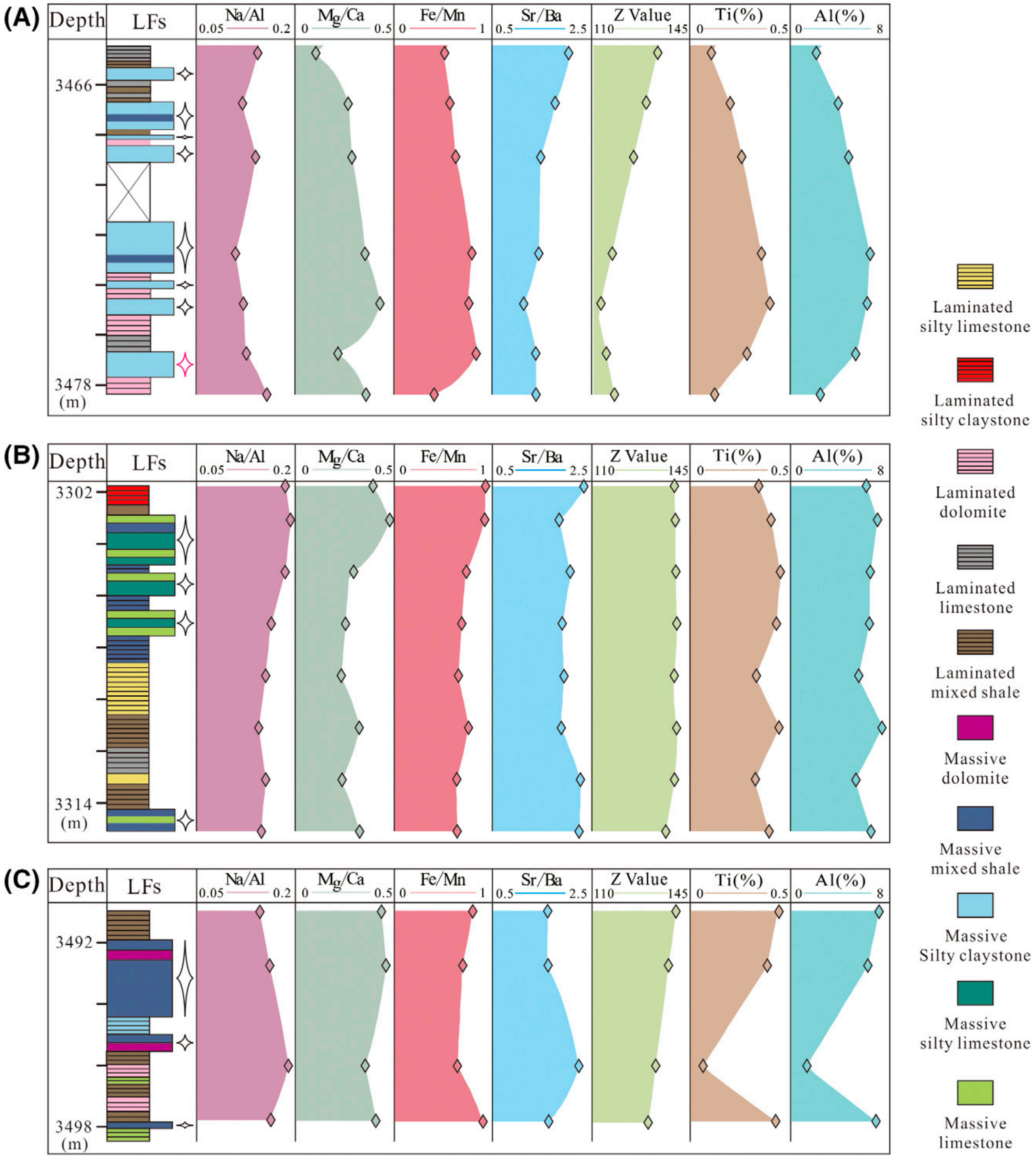

Figure 18. Distribution of lithofacies and sedimentary environment characteristics of massive shales. (A) Massive calcareous shale, well NY1, 3302–3315 m. (B) Massive claystone, well NY1, 3465–3468 m. (C) Massive dolomitic shale, well NY1, 3491–3498 m. LFs = lithofacies; Z Value = salinity index Z value (calculated using carbon and oxygen isotopes).

formed by differences in seasonal sedimentation, note that they can also form during the deposition process. Physical simulation experiments and modern sedimentary records suggest that the flattening floc ripples, turbidite mudstone, and wave-enhanced sediment gravity flows can form a low-angle cross-bedding, which can form a “postulated lamina bedding” after compaction and dehydration (Schieber et al., 2007, 2013; Schieber and Southard, 2009; Macquaker et al., 2010; Plint, 2014; Yawar and Schieber, 2017). In the sedimentary

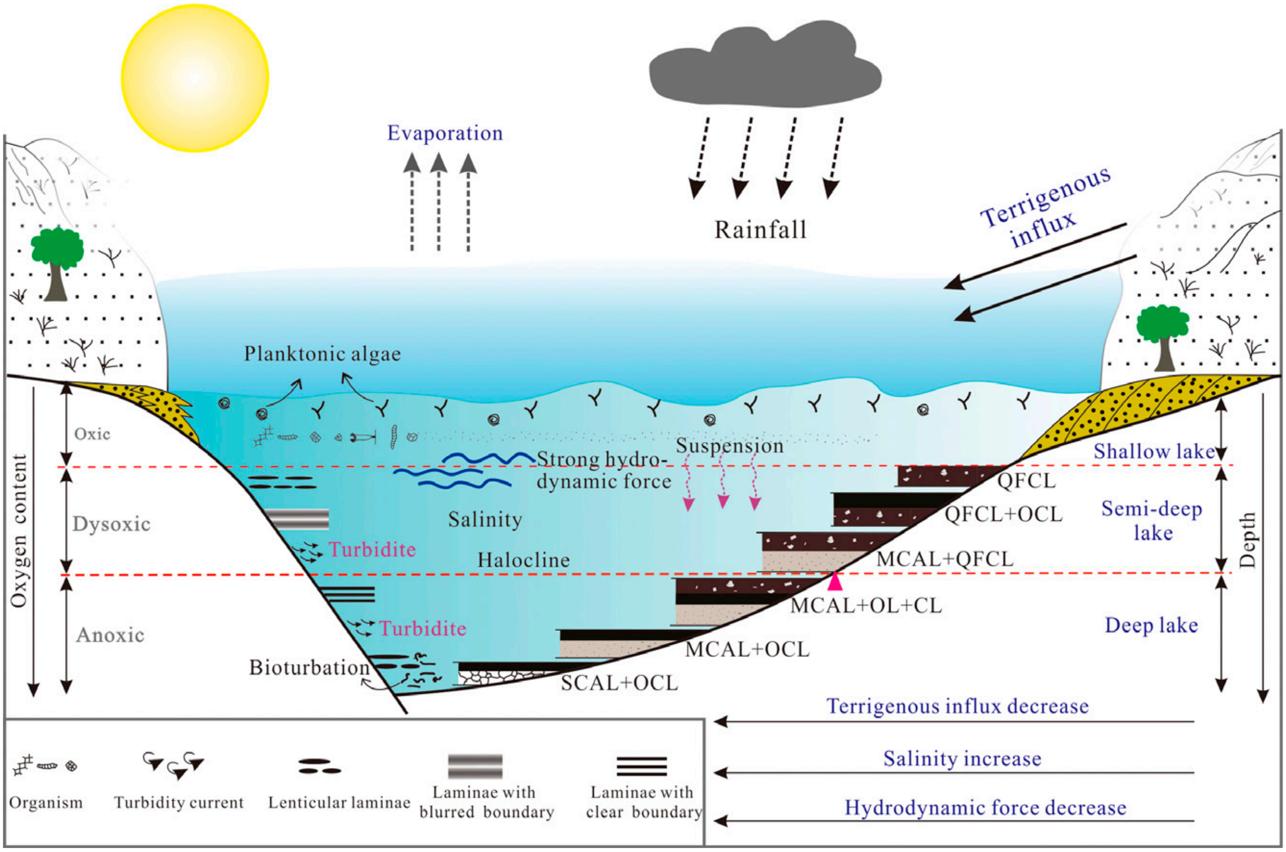

Figure 19. Depositional model of lacustrine carbonate-rich shale in the Eocene Jiyang depression. CL = clay laminae; MCAL = micritic calcite laminae; OCL = organic-rich clay laminae; OL = organic matter laminae; QFCL = quartz–feldspar–clay mixed laminae; SCAL = sparry calcite laminae.

records of shale, identifying different varve origin types is difficult. The integrated analysis of sedimentary backgrounds along with high-resolution sedimentary geochemical characteristics, sedimentary structures, and biological disturbance analysis as well as sedimentary processes analysis are useful.

The lacustrine shale records in East Asia provide an important opportunity for understanding the terrestrial ecological response to global climate change during this period. Moreover, the scale of the terrestrial lake basin is considerably smaller than that of the ocean; thus, it is more sensitive to the response of the tectonic-climate terrigenous input and the water body (Leng and Marshall, 2004; Li et al., 2018; Zou et al., 2019). Subsequently, lacustrine shale is characterized by high-frequency variations in the vertical and spatial distributions. The deposition rate depends on the sediment supply differences caused by seasonal climate, and extraction of the seasonal climate information in the lacustrine laminae can help in the analysis of the sedimentary records of climate change in the warm Eocene period in the midlatitudes (Pross et al., 2012; Wang et al., 2020). Although accurately identifying and extracting the seasonal sedimentary records is difficult, they are necessary for predicting future climate changes.

CONCLUSIONS

1. The lacustrine shale of the Es4s–Es3x formation is laminated, massive, and lenticular. Seven lamina units have been identified: MCAL, SCAL, QFCL, OCL, OL, CL, DL, and AL. They form seven types of LCs: MCAL + OL + CL, QFCL + OCL, SCAL + OCL, SCAL + OL, MCAL + QFCL, DL + OCL, and DL + AL. Additionally, three massive lithofacies have been identified: M1, M2, and M3. Three calcite lenticular laminae have also been identified.
2. Geochemical elements analysis shows that the Es4s–Es3x shale was deposited in a hypoxic

saline lake. Factors such as lake water, salinity, oxidation reduction, and water depth all vary with episodic high frequencies.

3. The lithology, lithofacies sequence, and geochemical characteristics indicate that the laminated shale was deposited via suspension. The halocline in the lake is a key factor that controls the lacustrine laminae deposition and LC distribution in the lake basin, which stems from the "water depth–terrigenous input" dynamic equilibrium.
4. The massive mudstone was formed due to turbidity, debris flows, and evaporation. The deposited MCAL may be due to the breakdown and resuspension of the massive mudstone under strong hydrodynamics. Erosion, deposition, and compaction of the water-rich muds and biodisturbance control the formation of the three lenses.
5. Lacustrine shales have complex depositional processes, and their deposition rates can vary by a factor of 10 or more. Therefore, we need to exclude the nonsuspended deposited shales as much as possible when performing paleoclimate reconstruction and obtaining isochronous stratigraphic sequences. Thus, accurately identifying and extracting the seasonal sedimentary records seems to be a requisite for predicting future climate change.

REFERENCES CITED

Algeo, T. J., and E. Ingall, 2007, Sedimentary C_{org}:P ratios, paleocean ventilation, and Phanerozoic atmospheric pO_2: Palaeogeography, Palaeoclimatology, Palaeoecology, v. 256, no. 3–4, p. 130–155, doi:10.1016/j.palaeo.2007.02.029.

Algeo, T. J., and C. Li, 2020, Redox classification and calibration of redox thresholds in sedimentary systems: Geochimica et Cosmochimica Acta, v. 287, p. 8–26, doi:10.1016/j.gca.2020.01.055.

Algeo, T. J., and J. Liu, 2020, A re-assessment of elemental proxies for paleoredox analysis: Chemical Geology, v. 540, 119549, 12 p., doi:10.1016/j.chemgeo.2020.119549.

Algeo, T. J., and J. B. Maynard, 2004, Trace-element behavior and redox facies in core shales of Upper Pennsylvanian Kansas-type cyclothems: Chemical Geology, v. 206, no. 3–4, p. 289–318, doi:10.1016/j.chemgeo.2003.12.009.

Aplin, A. C., and J. H. S. Macquaker, 2011, Mudstone diversity: Origin and implications for source, seal, and reservoir properties in petroleum systems: AAPG Bulletin, v. 95, no. 12, p. 2031–2059, doi:10.1306/03281110162.

Arthur, M. A., and B. B. Sageman, 1994, Marine black mudstones: Depositional mechanism and environments of ancient deposits: Annual Review of Earth and Planetary Sciences, v. 22, no. 1, p. 499–551, doi:10.1146/annurev.ea.22.050194.002435.

Burke, I. T., I. Grigorov, and A. E. S. Kemp, 2002, Microfabric study of diatomaccous and lithogenic deposition in laminated sediments from the Gotland Deep, Baltic Sea: Marine Geology, v. 183, no. 1–4, p. 89–105, doi:10.1016/S0025-3227(01)00250-X.

Burton, D., K. Woolf, and B. Sullivan, 2014, Lacustrine depositional environments in the Green River Formation, Uinta Basin: Expression in outcrop and wireline logs: AAPG Bulletin, v. 98, no. 9, p. 1699–1715, doi:10.1306/03201413187.

Cao, J., L. W. Xia, T. T. Wang, D. M. Zhi, Y. Tang, and W. W. Li, 2020, An alkaline lake in the Late Paleozoic Ice Age (LPIA): A review and new insights into paleoenvironment and petroleum geology: Earth-Science Reviews, v. 202, 103091, 17 p., doi:10.1016/j.earscirev.2020.103091.

Charles, M. J., and M. S. Simmons, 1986, Methods for the determination of carbon in soils and sediments: A review: Analyst, v. 111, no. 4, p. 385–390.

Cheel, R. J., 1990, Horizontal lamination and the sequence of bed phases and stratification under upper-flow-regime conditions: Sedimentology, v. 37, no. 3, p. 517–529, doi:10.1111/j.1365-3091.1990.tb00151.x.

Chen, Z. H., W. B. Jian, L. Y. Zhang, and M. Zha, 2018, Organic matter, mineral composition, pore size, and gas sorption capacity of lacustrine mudstones: Implications for the shale oil and gas exploration in the Dongying depression, eastern China: AAPG Bulletin, v. 102, no. 8, p. 1565–1600, doi:10.1306/0926171423117184.

Deocampo, D. M., P. A. Berry, E. J. Beverly, G. M. Ashley, and R. E. Jarrett, 2017, Whole-rock geochemistry tracks precessional control of Pleistocene lake salinity at Olduvai Gorge, Tanzania: A record of authigenic clays: Geology, v. 45, no. 8, p. 683–686.

Ebert, T., and M. H. Trauth, 2015, Semi-automated detection of annual laminae (varves) in lake sediments using a fuzzy logic algorithm: Palaeogeography, Palaeoclimatology, Palaeoecology, v. 435, p. 272–282, doi:10.1016/j.palaeo.2015.05.024.

Frébourg, G., S. C. Ruppel, R. G. Loucks, and J. Lambert, 2016, Depositional controls on sediment body architecture in the Eagle Ford/Boquillas system: Insights from outcrops in west Texas, United States: AAPG Bulletin, v. 100, no. 4, p. 657–682, doi:10.1306/12091515101.

Ghadeer, S. G., and J. H. S. Macquaker, 2011, Sediment transport processes in an ancient mud-dominated succession: A comparison of processes operating in marine offshore settings and anoxic basinal environments: Journal of the Geological Society, v. 168, no. 5, p. 1121–1132, doi:10.1144/0016-76492010-016.

Hatch, J. R., and J. S. Leventhal, 1992, Relationship between inferred redox potential of the depositional environment and geochemistry of the Upper Pennsylvanian (Missourian) Stark Shale Member of the Dennis Limestone, Wabaunsee County, Kansas, U.S.A.: Chemical Geology,

v. 99, no. 1–3, p. 65–82, doi:10.1016/0009-2541(92)90031-Y.

Ilgen, A. G., J. E. Heath, I. Y. Akkutlu, L. T. Bryndzia, D. R. Cole, Y. K. Kharaka, T. J. Kneafsey, K. L. Milliken, L. J. Pyrak-Nolte, and R. Suarez-Rivera, 2017, Shales at all scales: Exploring coupled processes in mudrocks: Earth-Science Reviews, v. 166, p. 132–152, doi:10.1016/j.earscirev.2016.12.013.

Jokinen, S. A., J. J. Virtasalo, A. T. Kotilainen, and T. Saarinen, 2015, Varve microfabric record of seasonal sedimentation and bottom flow-modulated mud deposition in the coastal northern Baltic Sea: Marine Geology, v. 366, p. 79–96, doi:10.1016/j.margeo.2015.05.003.

Konitzer, S. F., S. J. Davies, M. H. Stephenson, and M. J. Leng, 2014, Depositional controls on mudstone lithofacies in a basinal setting: Implications for the delivery of sedimentary organic matter: Journal of Sedimentary Research, v. 84, no. 3, p. 198–214, doi:10.2110/jsr.2014.18.

Kotilainen, A., H. Vallius, and D. Ryabchuk, 2007, Seafloor anoxia and modern laminated sediments in coastal basins of the Eastern Gulf of Finland, Baltic Sea, *in* H. Vallius, ed., Holocene sedimentary environment and sediment geochemistry of the Eastern Gulf of Finland, Baltic Sea: Espoo, Finland, Geological Survey of Finland Special Paper 45, p. 49–62.

Lazar, O. R., K. M. Bohacs, J. H. S. Macquaker, J. Schieber, and T. M. Demko, 2015, Capturing key attributes of fine-grained sedimentary rocks in outcrops, cores, and thin sections: Nomenclature and description guidelines: Journal of Sedimentary Research, v. 85, p. 230–246, doi:10.2110/jsr.2015.11.

Leng, M. J., and J. D. Marshall, 2004, Palaeoclimate interpretation of stable isotope data from lake sediment archives: Quaternary Science Reviews, v. 23, no. 7–8, p. 811–831, doi:10.1016/j.quascirev.2003.06.012.

Li, L., D. K. Zhong, and M. X. Shi, 2007, Cenozoic uplifting/subsidence coupling between the west Shandong Rise and the Jiyang Depression, northern China [in Chinese with English abstract]: Acta Geologica Sinica, v. 81, p. 1215–1228.

Li, M. S., L. R. Kump, L. A. Hinnov, and M. E. Mann, 2018, Tracking variable sedimentation rates and astronomical forcing in Phanerozoic paleoclimate proxy series with evolutionary correlation coefficients and hypothesis testing: Earth and Planetary Science Letters, v. 501, p. 165–179, doi:10.1016/j.epsl.2018.08.041.

Li, Z. Y., J. Schieber, and P. K. Pedersen, 2021, On the origin and significance of composite particles in mudstones: Examples from the Cenomanian Dunvegan Formation: Sedimentology, v. 68, no. 2, p. 737–754, doi:10.1111/sed.12801.

Liang, C., Z. X. Jiang, Y. C. Cao, J. Wu, Y. S. Wang, and F. Hao, 2018, Sedimentary characteristics and origin of lacustrine organic-rich shales in the salinized Eocene Dongying Depression: GSA Bulletin, v. 130, no. 1–2, p. 154–174, doi:10.1130/B31584.1.

Lin, Z. L., H. Wang, H. Jiang, Y. Yue, G. Q. Xiao, and B. Zhang, 2009, The association analysis of tectonic stress field on episodic rifting in Cenozoic of Beitang Sag of Bohai Bay Basin [in Chinese with English abstract]: Journal of Oil and Gas Technology, v. 31, p. 24–29.

Liu, Q., L. Y. Zhang, Z. M. Shen, X. X. Kong, and Z. Li, 2004, Evolution of lake-basin types and occurrence of hydrocarbon source rocks in Dongying Depression [in Chinese with English abstract]: Acta Petrolei Sinica, v. 25, p. 42–45.

Loucks, R. G., and S. C. Ruppel, 2007, Mississippian Barnett Shale: Lithofacies and depositional setting of a deep-water shale-gas succession in the Fort Worth Basin, Texas: AAPG Bulletin, v. 91, no. 4, p. 579–601, doi:10.1306/11020606059.

Macquaker, J. H. S., and A. E. Adams, 2003, Maximizing information from fine-grained sedimentary rocks: An inclusive nomenclature for mudstones: Journal of Sedimentary Research, v. 73, no. 5, p. 735–744, doi:10.1306/012203730735.

Macquaker, J. H. S., S. J. Bentley, and K. M. Bohacs, 2010, Wave-enhanced sediment-gravity flows and mud dispersal across continental shelves: Reappraising sediment transport processes operating in ancient mudstone successions: Geology, v. 38, no. 10, p. 947–950, doi:10.1130/G31093.1.

Macquaker, J. H. S., K. G. Taylor, and R. L. Gawthorpe, 2007, High-resolution facies analyses of mudstones: Implications for paleoenvironmental and sequence-stratigraphic interpretations of offshore ancient mud-dominated successions: Journal of Sedimentary Research, v. 77, no. 4, p. 324–339, doi:10.2110/jsr.2007.029.

Milliken, K., 2014, A compositional classification for grain assemblages in fine-grained sediments and sedimentary rocks: Journal of Sedimentary Research, v. 84, no. 12, p. 1185–1199, doi:10.2110/jsr.2014.92.

Ochoa, J., J. Wolak, and M. H. Gardner, 2013, Recognition criteria for distinguishing between hemipelagic and pelagic mudrocks in the characterization of deep-water reservoir heterogeneity: AAPG Bulletin, v. 97, no. 10, p. 1785–1803, doi:10.1306/04221312086.

Ojala, A. E. K., P. Francus, B. Zolitschka, M. Besonen, and S. F. Lamoureux, 2012, Characteristics of sedimentary varve chronologies - A review: Quaternary Science Reviews, v. 43, p. 45–60, doi:10.1016/j.quascirev.2012.04.006.

Petter, A. L., and R. J. Steel, 2006, Hyperpycnal flow variability and slop organization on an Eocene shelf margin, Central Basin, Spitsbergen: AAPG Bulletin, v. 90, no. 10, p. 1451–1472, doi:10.1306/04240605144.

Piper, D. Z., and S. E. Calvert, 2009, A marine biogeochemical perspective on black shale deposition: Earth-Science Reviews, v. 95, no. 1–2, p. 63–96, doi:10.1016/j.earscirev.2009.03.001.

Plint, A. G., 2014, Mud dispersal across a Cretaceous prodelta: Storm-generated, wave-enhanced sediment gravity flows inferred from mudstone microtexture and microfacies: Sedimentology, v. 61, no. 3, p. 609–647, doi:10.1111/sed.12068.

Pross, J., L. Contreras, P. K. Bijl, D. R. Greenwood, S. M. Bohaty, S. Schouten, J. A. Bendle, et al., 2012, Persistent near-tropical warmth on the Antarctic continent during the early Eocene epoch: Nature, v. 488, no. 7409, p. 73–77, doi:10.1038/nature11300.

Qiu, N. S., X. G. Su, Z. Y. Li, Z. Q. Liu, and Z. Li, 2006, The Cenozoic tectono-thermal evolution of Jiyang depression, Bohai Bay Basin, East China [in Chinese with English abstract]: Chinese Journal of Geophysics, v. 49, no. 4, p. 1015–1024, doi:10.1002/cjg2.923.

Ren, J. Y., and Q. L. Zhang, 2004, Analysis of development mechanism for center uplift belt in Dongying Depression: Geotectonica et Metallogenia, v. 28, p. 254–262.

Rimstidt, J. D., J. A. Chermak, and M. E. Schreiber, 2017, Processes that control mineral and element abundances in shales: Earth-Science Reviews, v. 171, p. 383–399, doi:10.1016/j.earscirev.2017.06.010.

Roop, H. A., G. B. Dunbar, R. Levy, M. J. Vandergoes, A. L. Forrest, S. L. Walker, J. Purdie, P. Upton, and J. Whinney, 2015, Seasonal controls on sediment transport and deposition in Lake Ohau, South Island, New Zealand: Implications for a high-resolution Holocene palaeoclimate reconstruction: Sedimentology, v. 62, no. 3, p. 826–844, doi:10.1111/sed.12162.

Schieber, J., 2011, Reverse engineering mother nature-shale sedimentology from an experimental perspective: Sedimentary Geology, v. 238, no. 1–2, p. 1–22, doi:10.1016/j.sedgeo.2011.04.002.

Schieber, J., 2016, Experimental testing of the transport-durability of shale lithics and its implications for interpreting the rock record: Sedimentary Geology, v. 331, p. 162–169, doi:10.1016/j.sedgeo.2015.11.006.

Schieber, J., and J. B. Southard, 2009, Bedload transport of mud by floccule ripples–Direct observation of ripple migration processes and their implications: Geology, v. 37, no. 6, p. 483–486, doi:10.1130/G25319A.1.

Schieber, J., J. B. Southard, P. Kissling, B. Rossman, and R. Ginsburg, 2013, Experimental deposition of carbonate mud from moving suspensions: Importance of flocculation and implications for modern and ancient carbonate mud deposition: Journal of Sedimentary Research, v. 83, no. 11, p. 1026–1032, doi:10.2110/jsr.2013.77.

Schieber, J., J. B. Southard, and A. Schimmelmann, 2010, Lenticular shale fabrics resulting from intermittent erosion of water-rich muds–Interpreting the rock record in the light of recent flume experiments: Journal of Sedimentary Research, v. 80, p. 119–128, doi:10.2110/jsr.2010.005.

Schieber, J., J. Southard, and K. Thaisen, 2007, Accretion of mudstone beds from migrating floccule ripples: Science, v. 318, no. 5857, p. 1760–1763, doi:10.1126/science.1147001.

Schimmelmann, A., C. B. Lange, J. Schieber, P. Francus, A. E. K. Ojala, and B. Zolitschka, 2016, Varves in marine sediments: A review: Earth-Science Reviews, v. 159, p. 215–246, doi:10.1016/j.earscirev.2016.04.009.

Shi, J. Y., Z. J. Jin, Q. Y. Liu, Z. K. Huang, and Y. Q. Hao, 2018, Terrestrial sedimentary responses to astronomically forced climate changes during the Early Paleogene in the Bohai Bay Basin, eastern China: Palaeogeography, Palaeoclimatology, Palaeoecology, v. 502, p. 1–12, doi:10.1016/j.palaeo.2018.01.006.

Shi, J. Y., Z. J. Jin, Q. Y. Liu, R. Zhang, and Z. K. Huang, 2019, Cyclostratigraphy and astronomical tuning of the middle Eocene terrestrial successions in the Bohai Bay Basin, Eastern China: Global and Planetary Change, v. 174, p. 115–126, doi:10.1016/j.gloplacha.2019.01.001.

Soyinka, O. A., and R. M. Slatt, 2008, Identification and micro-stratigraphy of hyperpycnites and turbidites in Cretaceous Lewis Shale, Wyoming: Sedimentology, v. 55, no. 5, p. 1117–1133, doi:10.1111/j.1365-3091.2007.00938.x.

Stow, D. A. V., and A. J. Bowen, 1980, Physical model for the transport and sorting of fine-grained sediment by turbidity currents: Sedimentology, v. 27, no. 1, p. 31–46, doi:10.1111/j.1365-3091.1980.tb01156.x.

Stow, D. A. V., A. Y. Huc, and P. Bertrand, 2001, Depositional processes of black shales in deep water: Marine and Petroleum Geology, v. 18, no. 4, p. 491–498, doi:10.1016/S0264-8172(01)00012-5.

Stow, D. A. V., and M. Mayall, 2000, Deep-water sedimentary systems New models for the 21st century: Marine and Petroleum Geology, v. 17, no. 2, p. 125–135, doi:10.1016/S0264-8172(99)00064-1.

Tänavsuu-Milkeviciene, K., and J. F. Sarg, 2012, Evolution of an organic-rich lake basin-stratigraphy, climate and tectonics: Piceance Creek basin, Eocene Green River Formation: Sedimentology, v. 59, no. 6, p. 1735–1768, doi:10.1111/j.1365-3091.2012.01324.x.

Thiry, M., 2000, Paleoclimatic interpretation of clay minerals in marine deposits: An outlook from the continental origin: Earth-Science Reviews, v. 49, no. 1–4, p. 201–221, doi:10.1016/S0012-8252(99)00054-9.

Tindall, J., R. Flecker, P. Valdes, D. N. Schmidt, P. Markwick, and J. Harris, 2010, Modelling the oxygen isotope distribution of ancient seawater using a coupled ocean-atmosphere GCM: Implications for reconstructing early Eocene climate: Earth and Planetary Science Letters, v. 292, no. 3–4, p. 265–273, doi:10.1016/j.epsl.2009.12.049.

Wang, M., H. H. Chen, C. J. Huang, D. B. Kemp, T. W. Xu, H. A. Zhang, and M. S. Li, 2020, Astronomical forcing and sedimentary noise modeling of lake level changes in the Paleogene Dongpu Depression of North China: Earth and Planetary Science Letters, v. 535, 116116, 13 p., doi:10.1016/j.epsl.2020.116116.

Watanabe, H., and M. Akiyama, 1998, Characterization of organic matter in the Miocene turbidites and hemipelagic mudstones in the Niigata oil field, central Japan: Organic Geochemistry, v. 29, no. 1–3, p. 605–611, doi:10.1016/S0146-6380(98)00082-5.

Wei, W., and T. J. Algeo, 2020, Elemental proxies for paleosalinity analysis of ancient shales and mudrocks: Geochimica et Cosmochimica Acta, v. 287, p. 341–366, doi:10.1016/j.gca.2019.06.034.

Wei, W., T. J. Algeo, Y. Lu, Y. Lu, H. Liu, S. Zhang, L. Peng, J. Zhang, and L. Chen, 2018, Identifying marine incursions into the Paleogene Bohai Bay Basin lake system in northeastern China: International Journal of Coal Geology, v. 200, p. 1–17, doi:10.1016/j.coal.2018.10.001.

Wittkop, C. A., J. L. Teranes, W. E. Dean, and T. P. Guilderson, 2009, A lacustrine carbonate record of Holocene seasonality and climate: Geology, v. 37, no. 8, p. 695–698, doi:10.1130/G30056A.1.

Xia, L. W., J. Cao, S. Z. Hu, and S. F. Li, 2019a, How marine incursion influences the quality of lacustrine source rocks: The Paleogene Nanxiang Basin, eastern China: AAPG Bulletin, v. 103, no. 5, p. 1071–1096, doi:10.1306/101261817268.

Xia, L. W., J. Cao, S. Z. Hu, S. F. Li, and C. H. Shi, 2019b, Organic geochemistry, petrology, and conventional and unconventional hydrocarbon resource potential of Paleogene saline source rocks in eastern China: The Biyang Sag of the Nanxiang Basin: Marine and Petroleum Geology, v. 101, p. 343–354, doi:10.1016/j.marpetgeo.2018.11.032.

Yang, H. Z., J. Ren, and J. B. Lu, 2009, Tectonic styles and kinematic characteristics of negative inversion structure in Dongying Depression: Earth Science-Journal of China University of Geosciences, v. 34, p. 493–501.

Yawar, Z., and J. Schieber, 2017, On the origin of silt laminae in laminated shales: Sedimentary Geology, v. 360, p. 22–34, doi:10.1016/j.sedgeo.2017.09.001.

Zolitschka, B., A. Brauer, J. F. W. Negendank, H. Stockhausen, and A. Lang, 2000, Annually dated late Weichselian continental paleoclimate record from the Eifel, Germany: Geology, v. 28, no. 9, p. 783–786, doi:10.1130/0091-7613(2000)28<783:ADLWCP>2.0.CO;2.

Zolitschka, B., and D. Enters, 2009, Lacustrine sediments, *in* V. Gornitz, ed., Encyclopedia of paleoclimatology and ancient environments: Dordrecht, the Netherlands, Springer, p. 486–488, doi:10.1007/978-1-4020-4411-3_120.

Zolitschka, B., P. Francus, A. E. K. Ojala, and A. Schimmelmann, 2015, Varves in lake sediments: A review: Quaternary Science Reviews, v. 117, p. 1–41, doi:10.1016/j.quascirev.2015.03.019.

Zou, C. N., R. K. Zhu, Z. Q. Chen, J. G. Ogg, S. T. Wu, D. Z. Dong, Z. Qiu, et al., 2019, Organic-matter-rich shales of China: Earth-Science Reviews, v. 189, p. 51–78, doi:10.1016/j.earscirev.2018.12.002.